MOUNTAIN-PLAINS CONSORTIUM

MPC 18-345 | H. Mahmoud and H. Wen

A Modified Approach for Predicting Fracture of Steel Components Under Combined Large Inelastic Axial and Shear Strain Cycles

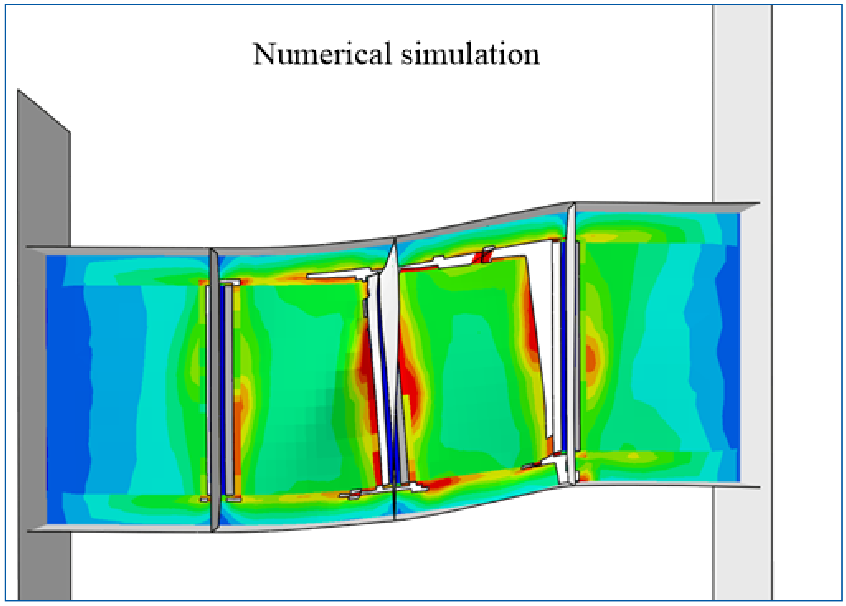

A University Transportation Center sponsored by the U.S. Department of Transportation serving the Mountain-Plains Region. Consortium members:

Colorado State University
North Dakota State University
South Dakota State University
University of Colorado Denver
University of Denver
University of Utah
Utah State University
University of Wyoming

A Modified Approach for Predicting Fracture of Steel Components under Combined Large Inelastic Axial and Shear Strain Cycles

by

Hussam Mahmoud (PI)
Huajie Wen

Department of Civil and Environmental Engineering
Colorado State University
Fort Collins, CO 80523

April 2018

Acknowledgement

The funds for this study were provided, in part, by the United States Department of Transportation to the Mountain-Plains Consortium (MPC). Matching funds were provided by Colorado State University. The data for this study was provided by Colorado State Patrol and Colorado Department of Transportation, which is greatly appreciated.

ABSTRACT

Separation of material, known as fracture, is one of the ultimate failure phenomena in steel elements. Preventing or delaying fracture is therefore essential for ensuring structural robustness under extreme demands. Despite the importance of fracture as the final stage during inelastic response of elements, the underlying mechanisms and the factors influencing the onset and progression of fracture have not been fully investigated. This is particularly the case for ductile fracture where significant pre-crack deformations are present. Existing approaches geared at predicting brittle fracture, marked by little to no plastic deformation, have been proven inadequate for capturing ductile fracture. Ductile fracture is dependent on two stress state parameters, the stress triaxiality and Lode parameter, which correspond, respectively, to two kinds of work hardening damage, which are hydrostatic and deviatoric stress components. The role of stress triaxiality on ductile fracture has been well defined and implemented in various models over the past several decades. Only until recently, however, has the role of Lode parameter been identified as an important factor for accurate prediction of ductile fracture. In general, no reliable fracture prediction methods are present that are consistent throughout the whole range of stress states, where the stresses are dominated by either tension loading, shear loading, or a combination of both.

In this study, a new ductile fracture criterion based on monotonic loading conditions is first developed based on analysis and definitions of the two stress state parameters and subsequently extended to the reverse/cyclic loading conditions. The extension from monotonic to cyclic loading is based fundamentally on the fact that as long as large pre-crack plastic strain fields exist, the inherent mechanism in both loading cases can be viewed as the same. Although the inherent mechanism is the same for both loading cases, extending the model to the reverse loading conditions required the inclusion of the effects of nonlinearity of the damage evolution rule as well as the loading history. The two criteria, monotonic and cyclic, are then validated on the coupon specimen level through comparisons between predicted fracture strains and their experimental equivalents for various metal types and steel grades that are available in the literature. The newly developed models offer improvements to existing known ductile fracture criteria in terms of both accuracy and practicality.

Following the validation of the fracture model on the coupon specimen level, the model is employed on the connection level, up to and including failure, to evaluate block shear failure for gusset plate and coped beam connections under monotonic loading and shear links under cyclic loading. The chosen connection types are dependent on stress triaxiality (tension) and Lode parameter (shear) and are therefore appropriate for the validation of the ductile fracture model. For the block shear failure, prediction accuracy is verified through comparisons with results from corresponding laboratory tests, in the perspective of load versus displacement curves, fracture profiles, and fracture sequences. Some underlying mechanism of block shear is also explored and explained for the first time. Following the same modeling procedure, parametric studies on geometric effects on block shear failure is conducted. Three different block-shear failure modes and one bolt hole tear out mode are captured in the simulations and suggestions on design code changes are provided. For the shear links, which are typically employed in eccentric braced frames, simulation of fracture under reverse/cyclic loading is also conducted and verifications are performed through comparisons with their previous experimental results. The fracture-associated variables are included in the cyclic loading analysis through deriving an implicit integration algorithm for the material constitutive equations with combined hardening, which was integrated in the simulation using a user-defined material subroutine VUMAT.

TABLE OF CONTENTS

LIST OF TABLES

LIST OF FIGURES

1. STATE OF ART ON FRACTURE OF STEEL UNDER COMBINED LARGE INELASTIC AXIAL AND SHEAR STRAIN CYCLES

1.1 Overview

Fracture of steel components after extensive plasticity and cyclic inelastic deformations is common under many extreme events. The failure usually occurs after very limited number of stress/strain cycles and is often categorized as ultra-low cycle fatigue (ULCF) or extreme-low cycle fatigue (ELCF). Large inelastic strains under extreme events are often desirable as a source of significant energy absorption with sufficient level of ductility. While steel as a material is known to be very ductile with ductility ratios as large as 50 to 100 (ductility ratio is the ratio of ultimate deformation to yield deformation), overreliance on ductility can lead to catastrophic consequences. For example, in the 1994 Northridge earthquake, many moment connections fractured in a brittle manner as a result of various design and fabrication defects.

Although numerous studies following the Northridge earthquake have been conducted in order to improve the resistance of steel structures to large cyclic loadings, research on predicting fracture resistance of components and details are scarce. Although several criteria have been proposed for predicting fatigue and fracture in metal components under large loading demand, the studies have only been geared exclusively toward cases with specific restraint conditions. In addition, attempts to extend existing low cycle fatigue criteria to the ULCF have proven to be neither accurate nor applicable. Furthermore, directly applying traditional fracture mechanics, such as the J-integral and Crack Tip Opening Displacement (CTOD), to cases of large inelastic strain reversals are also questionable. This is because the conventional fracture mechanics approaches are based on assuming the presence of an initial flaw with a highly constrained crack tip, limited plastic strain crack regions, and nonlinear elastic behavior.

Fracture under monotonic loading with large pre-crack plastic strains, which is often named as ductile fracture, can be viewed as a special case of “cyclic loading” with failure after a quarter cycle. The asymmetric stress state in the case of monotonic loading, in terms of the hydrostatic and deviatoric stress components, is the main contributor to the asymmetric damage in connections. However, existing fracture criteria employing hydrostatic and deviatoric stresses are either inapplicable to all stress state ranges or uneconomical in calibration and application to practical structural details. It is also arguable that since monotonic loading is a “special” case of cyclic loading, appropriate ULCF criteria should capture ductile fracture under monotonic loading.

The mechanisms of ULCF and monotonic ductile fracture are known to exhibit intrinsic similarities through numerous analyses on crack topology using fractographic analysis (Kanvinde and Deierlein, 2007). Therefore, ULCF can be viewed as series of combination of monotonic ductile fractures and their reversals. Thus, it is not too farfetched to presume that they also share similar crack formation characteristics, and that the extension of monotonic ductile fracture criteria to the case of reverse loading, specifically ULCF, merits extensive consideration.

Numerical simulations of structural components or systems through their full range of responses, including failure, under complex stress states are scarce. For instance, gusset plates and coped beams are one of the most popular and widely used connection components in steel structures. They are designed to transfer both tension and compression forces or tension and shear force, respectively. One of the predominant failure modes in these connections is block shear, which is due to tensile and shear stress states. The presence of both tension and shear stresses imposes challenges in numerical simulations of such failure, which is evident in the lack of agreement between existing numerical studies and experimental results. Therefore, the development of new and accurate fracture models and their applications to predicting the response of structural components and systems can yield significant dividends for understanding the failure mechanisms and the corresponding structural response.

1.2 Traditional Fracture Mechanics Approaches

Traditional fracture mechanics is based on the concept of the energy release rate, which is usually a function of a single parameter (e.g., stress intensity factor (K), J-integral, or CTOD), and thus used as a one-parameter fracture criterion under specific conditions. The basic concept is that cracks in solids will propagate when the strain energy released by the crack extension exceeds the energy required for creating a new crack surface. By the difference in the assumption made regarding the yield zone surrounding the crack tip, traditional fracture mechanics can be categorized into linear elastic fracture mechanics (LEFM) with limited yield zone and elastic-plastic fracture mechanics with noticeable yield zone, as further discussed in the following sections. Some of the basic concepts are summarized from Anderson (1995). Based on the linear elastic assumption, the stress conditions around a crack tip can be determined, for example, as an infinite plate with a crack length of 2a subjected to a far field axial stress σ normal to the crack. The stress intensity factor K_I for this mode can be determined by Equation 2.1 as follows:

$$K_I = \sigma\sqrt{\pi a}\ . \tag{1.1}$$

Since the LEFM assumption is invalid under large plastic behavior, several approaches with increased dominance zones have been developed, and which are referred to as “Elastic-Plastic Fracture Mechanics.” The most popular of which is the “J-integral” approach proposed by Rice (1968). The J-dominance zone is generally much larger than the K-dominance zone; hence, the J-integral approach is more applicable than LEFM in many situations involving large-scale yielding. CTOD was another approach widely explored explored even before Rice (1968) developed J-integral, mainly in the UK, and later identified to be, in fact, analogous to the J-integral (Anderson, 1995).

In these approaches, the energy release rate serves as the main and only quantity to characterize resistance to fracture under different loading conditions and thus the ability to absorb energy without fracturing has been introduced and named as “toughness.” Under different constraint conditions, such as three-dimensional constraint, the resistance to fracture varies where the fracture toughness decreases under plane strain and increases under plane stress. According to common definitions, further fracture will occur when the energy release rate exceeds the toughness of the material. However, in reality, the stress state governs the potential for fracture. Consequently, a one-to-one correspondence between the energy release rate and toughness is acceptable for traditional fracture mechanics under specific constraint conditions. However, such an approach is invalid in the presence of excessive pre-crack plasticity, in which toughness actually depends on the size and geometry of the specimens and may significantly vary throughout a loading history.

Another issue regarding the use of traditional fracture mechanics, in cases with excessive yielding at the crack tip, is the validity of the singularity assumption, which is challenged by the presence of crack tip blunting, which is due to large plasticization. The postulation of nonlinear elastic behavior in the J-integral leads to another issue. That is, when the crack grows, a plastic “wake” develops ahead of the crack as the crack moves forward. The wake area represents a region where the material has been plastically loaded and then elastically unloaded with residual plastic deformation, and hence the nonlinear elastic assumption violates such true material behavior.

If the plasticity remains confined to a relatively small region and the constraints are not low, the traditional fracture mechanic approaches are still the most popular and widely used because of their successful application in many practical situations over the years. However, if the plasticization grows larger, or there exists low level and more complex constraint conditions, the use of these traditional approaches is rather questionable.

Another issue regarding the use of traditional fracture mechanics approaches lies in their two-dimensional definition. It has been observed that thicker geometries are more prone to fracture, since there are larger constraints, and this effect cannot be considered by these approaches. Although there are approaches that attempt to add the additional stress constraints, such as the J-Q theory proposed by O'Dowd and Shih (1991), they are either difficult to apply or calibrate.

1.3 Traditional Fatigue Approaches

Fatigue failure can be defined as a series of fracture propagation when the material is subjected to cyclic loading. Depending on the number of cycles to failure, fatigue can be phenomenologically categorized as high-cycle fatigue and low-cycle fatigue. Repeated loadings are found to be very detrimental to materials with respect to stiffness and strength, even when the levels of stresses from the applied loads are far below the yield stress or ultimate strength.

The key question regarding fatigue strength is whether or not a crack will grow over a certain number of cycles. For some materials, when the cyclic stress range is below a certain value, the fatigue failure will not occur, and this value is usually called fatigue limit, endurance limit, or fatigue strength; but for some other material such threshold amplitude does not exist (Pyttel, et al., 2011). In the fracture mechanics framework, the limit is identified as the fatigue threshold, ΔK_{th}, below which the fatigue crack will not grow farther (ΔK_{th} is the change in stress-intensity factor threshold). When the stress range amplitude near the crack tip, defined by the change in stress intensity factor ΔK increases, the fatigue life decreases.

Currently there are two types of modeling methodology considered for simulating the relation between fatigue life and stress range amplitude during cyclic loading. The first approach is based on fatigue crack propagation in terms of ΔK, and the other is based on cumulative fatigue damage as a function of the amplitude of stresses and strains. The cumulative fatigue approaches are mostly phenomenological, while the crack propagation theories are more dependent on physical mechanisms.

1.3.1 Crack Propagation Approach

The basic concept for the crack propagation approach is that the crack growth increment at each cycle is calculated using a specific criterion, and once the crack grows to a critical length, the material is considered to have failed. The crack propagation rate is usually described as *da/dN*, where N is number of cycles, and such a rate is shown schematically in Figure. 1.1, which comprises the three stages. Paris et al. (1961) first employed fracture mechanics to predict regions of stable fatigue crack growth under high-cycle fatigue (Stage II). Since then, the "Paris Law," which is Equation 2.2, has become the main approach for assessing crack growth under a low magnitude stress range.

$$\frac{da}{dN} = A(\Delta K)^n \tag{1.2}$$

where A and n are material constants.

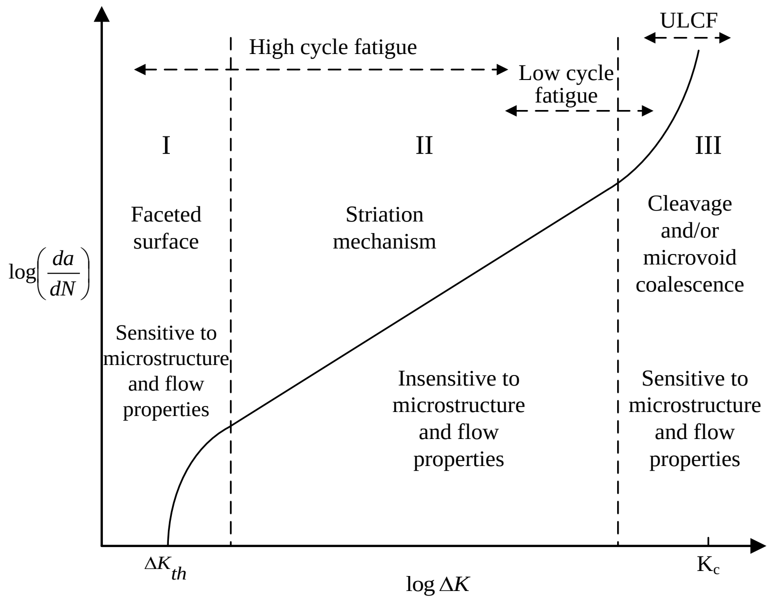

Figure 1.1 Stage and mechanisms of fatigue crack growth

In stage III, the crack growth rate indicates obvious acceleration, and the crack actually propagates in an unstable manner. In this stage the fracture process, such as the microvoid coalescence and cleavage, also plays a role in crack extension. The overall crack growth is driven by the combined effects from fatigue and static fracture mechanisms. The contributions from fatigue decreases with increases in the maximum stress intensity factor, K_{max}, and the failure mode gradually moves to complete monotonic fracture. Fracture under monotonic loadings, such as microvoid coalescence, cleavage, or both, are very sensitive to material properties, and hence such dependency is also high for stage III fatigue.

The main difference between fatigue failure and fracture under monotonic loadings lies in their different driving forces. In fatigue, a crack will grow in each eligible cycle with stress amplitude above the endurance limit. Meanwhile, under the same stress levels but without repeated loadings, fracture will not progress further. Hence, the loading cycle is one of the additional driving forces for fatigue compared to monotonic fracture, and such extra driving force arises from the sharpening process of the crack tip in the reversed half cycles. At the same time, when the stress/strain fields during cyclic loadings are so large, even if the cyclicity halts, crack growth still occurs.

For traditional fatigue failure, stage III does not play an important role since it takes a long time for a crack to grow from a small initial flaw to a critical size, and in such cases stage III probably only accounts for less than 1% of the total fatigue life. Studies on crack growth in region III is also scarce. For ULCF, stage III is the dominating phase, and typical fatigue theories do not apply. Under large loading demand, ULCF is the common failure mode, therefore modeling of this fatigue stage should be explored.

1.3.2 Cumulative Fatigue Damage Approach

Fatigue damage develops with applied load cycles in an accumulative manner, and thus the cumulative fatigue damage theory has been the traditional approach for fatigue life assessment. The most common approach is the “linear damage rule” (LDR), which assumes fatigue damage accumulates in a linear way, and is also known as Miner’s rule (Miner, 1957), expressed as

$$D = \sum_i \frac{n_i}{N_i} \qquad (1.3)$$

where n_i and N_i are the number of cycles and fatigue life, respectively, for the i th strain/stress range amplitude. Although many nonlinear rules have been developed to address the shortcomings of LDR, through more extensive considerations of the stress/strain amplitudes, such as load sequence and deformation history effects, LDR remains the simplest and most frequently used cumulative rule.

Fatigue damage is fundamentally the result of microstructural changes in the materials. Such changes on the microstructural level are assumed to have inherent relationships with macroscopic quantities, such as the stress (S-N Curve) and strain (Manson-Coffin model) (Manson, 1965, and Coffin, 1954). By employing different macroscopic quantities, various criteria have been derived in order to describe the cumulative fatigue damage evolution in the framework of LDR. The commonly used quantities, stress and strain, are briefly introduced in some representative models in the following sections. A comprehensive review on the use of other quantities, such as energy and continuum damage mechanics-based approaches, can be found in Fatemi and Yang (1998).

1.4 Ultra-low Cycle Fatigue Models

Studies on fracture predictions of stage III fatigue are relatively scarce. Fatigue at this stage is always featured with large plastic strain reversal, and thus the traditional stress-based fatigue approaches are not applicable to this stage. The number of cycles up to failure is usually less than 10 to 15 cycles since local strains are so large. In such case, crack propagation is more prone to fracture rather than fatigue.

1.4.1 Extensions from Traditional Fatigue Model

Traditional low cycle fatigue criteria, such as the strain-based approaches, only account for the fatigue part, and inevitably will gradually lose accuracy with the reduction in fatigue life. The predictions by applying the Manson-Coffin criterion coupled with Miner's rule to ULCF have been proven inaccurate (Kuroda, 2001; Tateishi, et al., 2007). As shown in Figure 1.2, as the plastic range $\Delta\varepsilon_p$ decreases, predictions by the Manson-Coffin criterion gradually start to overestimate the fatigue life, and the fracture also transfers from the surface fracture mode (fatigue) to the internal fracture mode (ductile fracture). In Figure 1.3, the Damage, D_{Miner}, at the final fracture calculated by Miner's rule at Equation 1.3 and the Manson-Coffin criterion is plotted, which gradually moves away from the supposed critical damage value "1" as the strain range increases.

There have been several attempts to extend the traditional low cycle fatigue to the ULCF by introducing a fracture damage portion to fatigue models (Du et al., 1992; Kuroda, 2001; Tateishi et al., 2007; Xue, 2008; et al.), but only limited success has been achieved thus far. One obvious problem for the extension from traditional fatigue to ULCF lies in the counting technique. Since strain ranges for a given loading history may significantly vary due to randomness in the loading history, the traditional cycle counting technique used for traditional fatigue life predictions will only give number of cycles to failure. This might provide some useful information, but cannot accurately indicate the onset of fracture caused by a large cycle that might have contributed the most to damage in an early stage or in a later stage. For ULCF, there might be only several cycles needed for failure, so the cycle counting method can lead to order of magnitudes higher estimates of the number of cycles. Another issue lies in the multi-axial fatigue problem, and it is highly possible that there are varied stress states in different cycles, but the fracture damage, which will be discussed in the following section, is highly dependent on the stress state. The extensions, however, provide little information on the effects of stress state. Also, since traditional fatigue models are developed under the assumption of few or small plastic deformation, the determination of fatigue damage in ULCF through these criteria is questionable.

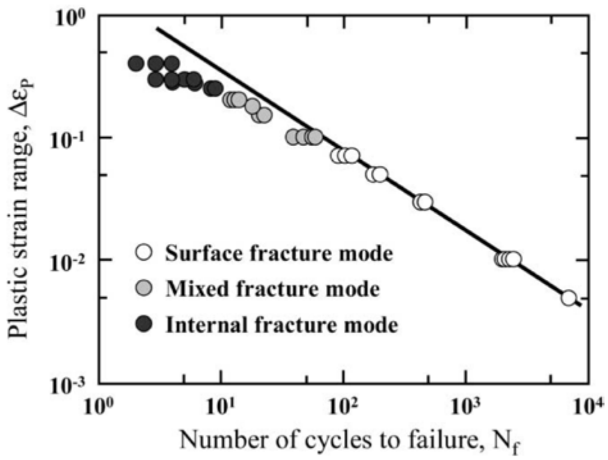

Figure 1.2 Fatigue life predictions versus real fatigue life (Kuroda, 2002)

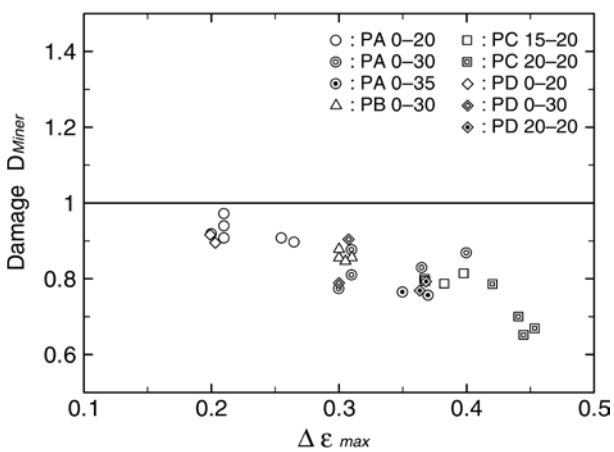

Figure 1.3 Relationship between the accumulated damage, D_{Miner}, and the maximum strain range $\Delta\varepsilon_{max}$ (Data from Tateishi et al., 2007)

1.4.2 Extension from Ductile Fracture Model

As previously stated, in the ULCF phenomenon, the fracture damage components gradually play a key role instead of the fatigue damage part, as has been previously indicated by Kuwamura and Yamamoto (1997). The fractographs of fracture surface in Kanvinde and Deierlein (2001), shown in Figure 1.4, indicates that both fracture surfaces of monotonic ductile fracture and ULCF are featured with dimpled profiles, which suggests that the underlying mechanism of ULCF is at least partially microvoid nucleation, growth, and coalescence. Therefore, it is logical to model ULCF starting from the pure ductile damage criterion that corresponds with monotonic loading. Actually, fracture under monotonic loading corresponds to a special case of ULCF, N ranges from 1/4 to 1/2, and in this case, the fatigue portion can be viewed as none.

Inspired by the significant fracture contribution, Kanvinde and Deierlein (2007) extended the Rice-Tracy ductile fracture model to cases with ULCF. The Cyclic Void Growth Model (CVGM) is shown as follows:

$$VGI_{cyclic} = \sum_{\text{tensile cycles}} \int \exp(1.5\eta) d\varepsilon_P - \sum_{\text{compressive cycles}} \frac{C_2}{C_1} \int \exp(1.5\eta) d\varepsilon_P \,, \tag{1.4}$$

$$VGI_{cyclic} = VGI_{monotonic} \exp\left(-\lambda \varepsilon_p^{accumulated}\right), \tag{1.5}$$

where η is the stress triaxiality, VGI is an abbreviation for Void Growth Indicator, C_1 and C_2 are material constants for VGM under tensile and compressive loading conditions, λ is the material constants for VGI degradation, and $\varepsilon_p^{accumulated}$ is the cumulative equivalent plastic strain excursion. The representative VGI evolution is shown in Figure 1.5 for the center of notched bar under cyclic loading.

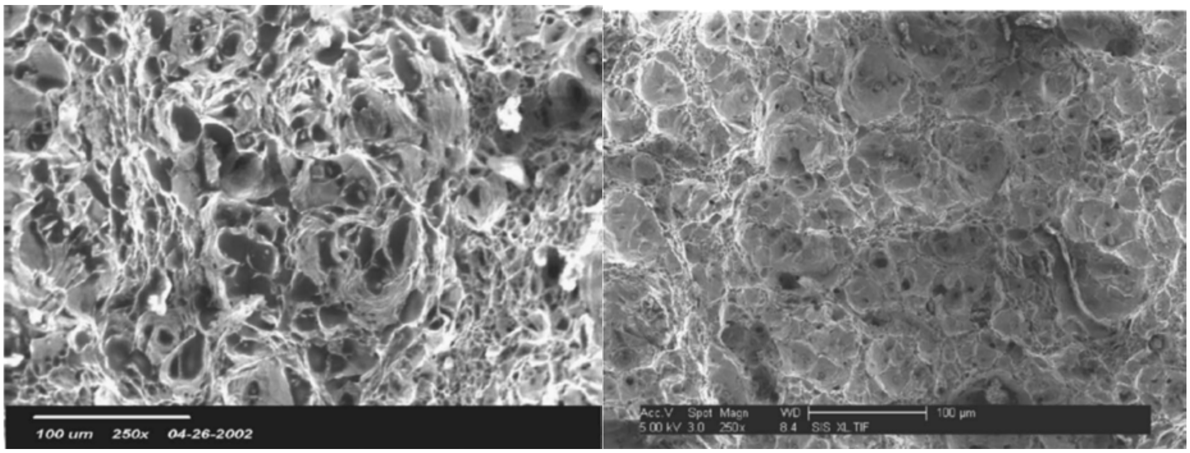

(a) (b)

Figure 1.4 Fractograph of fracture surfaces for AW50 steel: (a) Fracture under monotonic loading with deep dimples, and (b) Fracture after five loading cycles with shallower dimples. (Photos from Kanvinde and Deierlein, 2007)

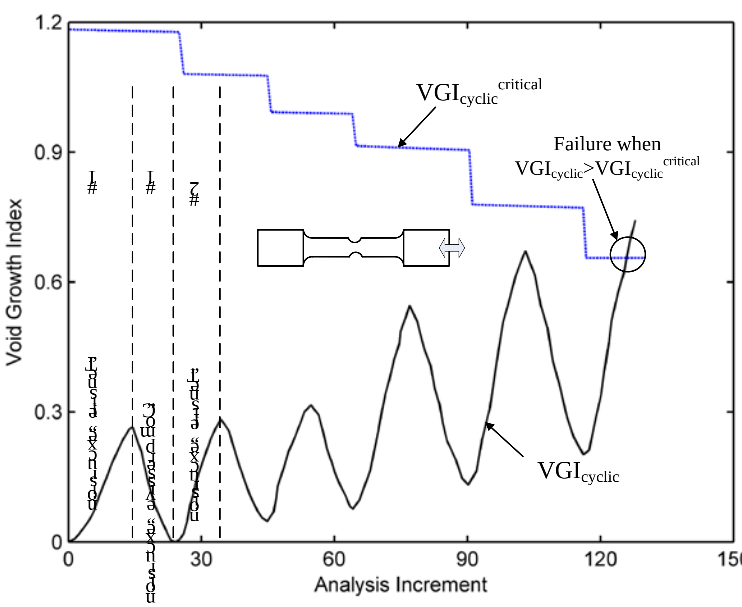

Figure 1.5 Damage evolution at the center of a notched bar during a cyclic loading history (Redrawn from Kanvinde and Deierlein, 2007)

The work by Kanvinde and Deierlein on extending ductile fracture to predict ULCF is indeed a creative idea. Some limitations, however, are worth noting to allow for proper extension of the model or the development of new models. First, VGI serves as the quasi-damage variable, but it is not an ever-increasing quantity, which contradicts many mainstream experiments and theories. Actually, in general terms, the damage variable, except for some special metals and under extreme large compressive loading, will not decrease. The VGI may only be viewed as a measure of porosity evolution, but the porosity itself is unable to reflect material conditions since the void volume is not the only influencing factor of fracture. Therefore, popular damage variables, such as the ductility measure, might be more suitable to predict fracture. In addition, only the stress triaxiality dependency in the ductile fracture model has been considered with some oversimplification in utilizing triaxiality, which lies in the fixed index 1.5 in Equation 1.4, which should be determined depending on many influencing factors, such as metal type and stress state. Another issue lies in the cyclic degradation, which physically should be viewed as a gradual process rather than a sudden phenomenon. Despite these shortcomings, if the model is only applied to mode I type loading in stage III fatigue, and if the stress triaxiality always lies in the intermediate to the high range, which mainly represents components under pure tensile and compressive cycles, acceptable results may be achieved.

1.4.3 Other Phenomenological Models

There have been many other phenomenological ULCF models. Some of the models of this type are derived from the strain energy related process. In these models, energy is used as a damage variable to predict failure in a member or component undergoing inelastic action under specific loading history. Damage is typically defined as the ratio of the energy dissipation in N cycles to the total energy dissipation until failure. Since phenomenological models are not directly related to this study, discussion on their advantages and disadvantages will not be provided.

1.5 Ductile Fracture Models

Inspired by the physical evolution of ductile fracture, the mechanism of voids nucleation, growth, and coalescence, numerous physical-based fracture models have been proposed under monotonic loading. Argon et al. (1975), Gurson (1977), Chu and Needleman (1980), Beremin (1981), Lee and Mear (1999), Benzerga and Leblond (2010) investigated and modeled the nucleation of voids; the foremost framework on voids growth was achieved by McClintock (1968), Rice and Tracey (1969), Gurson (1977), Tvergaard and Needleman (1984). The main findings on voids coalescence were introduced by Thomason (1968) and Tvergaard and Needleman (1984). In these physical-based models, the porosity is usually the only microstructural variable and often viewed as a damage indicator and the most widely used model, utilizing porosity as a damage indicator is the Gurson-Tvergaard-Needleman (GTN) model. Gologanu et al. (1993, 1994, and 1995) also introduced the void-shape change effect into porosity evolution and proposed the Gologanu-Leblond-Devaus (GLD) model. These porosity-based models, known as the Gurson-like models, are only sensitive to stress triaxiality. This means that the equivalent plastic strain to fracture is only dependent on the ratio of the first invariant of the stress tensor and the second invariant of the deviatoric stress tensor. Gurson-like models have gained a good reputation for describing predominant tensile fracture with moderate and high stress triaxiality. However, the models generally fail to predict fracture in the low and negative stress triaxiality domains, where shear fracture is believed to dominate. Various experimental data have confirmed that the shear effect, often expressed in terms of Lode parameters or the third invariant of the deviatoric stress tensor, also plays essential role in fracture formation and progression (Barsoum and Faleskog, 2007; Xue and Wierzbicki, 2008; Kiran and Khandelwal, 2014).

In parallel with these “physical-based” criteria, empirical ductile fracture models have also been proposed based on extensive experimental programs on bulk materials and sheets (Cockcroft and Latham, 1968; Brozzo et al., 1969; Oh et al., 1972; Oyane et al., 1980; Wilkins et al., 1980; Johnson and Cook, 1985; Clift et al., 1990; Ko et al., 2007). In the previously mentioned models, the effect of stress triaxiality is intrinsically considered since the data sets fall predominantly in the high stress triaxiality range. The loading cases with low and negative stress triaxialities were not comprehensively studied until the implementation of a series of experiments involving smooth and notched bars under complex tension and compression loading histories. The results of these tests are in Bao (2003), Bao and Wierzbicki (2004), Wierzbicki et al. (2005b), and Bai (2008). The experimental results from these tests, the recent experiments performed by Barsoum and Faleskog (2007), and the analytical model developed by Bai and Wierzbicki (2010) have all shown that both the Lode parameter and the stress triaxiality play an essential role in the prediction of strain and locus corresponding to ductile fracture.

The approach used for developing ductile fracture criterion can also be categorized into two groups: coupled and uncoupled approaches. In the coupled approach, the fracture criterion is coupled with a plasticity model and fracture is regarded as an accumulation process, which requires the inclusion of a damage evolution model. In the uncoupled approach, fracture is considered an abrupt phenomena and fracture suddenly occurs when the damage indicator, which is independent of the constitutive equations of material, reaches a critical limit. The most representative of the coupled criteria are the Gurson-like model and Lemaitre continuum damage model (Lemaitre, 1985). On the other hand, most empirical ductile fracture criteria can be viewed as uncoupled. Although some phenomenon prior to fracture, such as work softening, corresponds to the coupled criteria, most of fracture in structural components occurs in an abrupt manner, which is manifested by a sudden drop in the stress-versus-strain or load-versus-displacement curves. It is worth noting that the coupled constitutive and damage equations inevitably lead to extensive modeling and computational requirements, while the existing uncoupled constitutive equations have already been proven to be able to simulate material behavior with acceptable engineering accuracy. Hence, the uncoupled approach is adopted in the present study.

It is also worth noting that the previously highlighted studies mostly accommodated a specific range of stress states, and attempts to predict fracture using a unified equation are scarce. Therefore, developing a criterion that can be used in a wide range of stress states merits extensive study. Moreover, models for fracture with large pre-crack yielding under non-proportional loading, especially reverse loading, are limited, contrary to proportional loading in which the direction of the principal stresses remains constant and the ratios of their values are unchanged. Therefore, the development of such models is needed since failure is common in members or elements are subjected to large strain cycles. For example, failure of structural components under seismic loads is usually due to the concentration of large plastic stress/strain reversals for a short duration (i.e., ULCF). Since there are intrinsic similarities in crack topology formed under ULCF and monotonic loadings (i.e., uneven, dimple dominated surfaces exhibiting cup-and-cone profiles), the two fracture phenomena are believed to share similar crack formation characteristics, including void nucleation, growth, and coalescence. Therefore, extending monotonic fracture models to the case of reverse loading or ULCF appears to be a logical next step.

Classical fracture mechanics, in which the stress intensity factor, the J-integral, or the energy release rate is employed, provides reasonable solutions to stress-singularity problems when failure is characterized by brittle fracture. The Paris law is a typical example of the application of this kind of approach to the reverse/cyclic loading cases. However, the application of such criteria requires the existence of real or assumed initial flaws and highly constrained crack tips, as well as limited plastic strain crack regions, which are absent in many practical structural details.

Approaches in the framework of cumulative fatigue damage by means of direct stress and strain fields have also been proposed and applied to the prediction of fracture in brittle manners under reverse loading. The most well-known examples of such are the stress-based S-N curves developed for high cycle fatigue and the strain-based Manson-Coffin for low cycle fatigue. However, the use of such approaches is limited to material that has been subjected to a considerable number of cycles of reverse loading with limited pre-crack plastic strain. Attempts to apply the Manson-Coffin criterion to predict ULCF life have been proven inaccurate, and existing extension from ductile fracture cannot accommodate all ULCF situations.

Ductile fracture is only widely assessed in detailed study under monotonic and proportional loading cases; however, there is a lack of consideration of all influencing parameters in existing models. Moreover, the development of ductile fracture models under non-proportional loading, especially reverse loading, are limited, although failure of structural components under such loading is common. The mechanistic and physical differences between traditional LCF and ULCF also highlight the challenges for using LCF models for predicting ULCF life of components. Indeed, the extension from the ductile fracture model to the ULCF cases is the most promising solution.

2. NEW MODEL TO PREDICT FRACTURE OF STEEL

2.1 Description of Stress State

Ductile fracture models are usually expressed in terms of the stress invariants of the Cauchy stress tensor. Consider an arbitrary Cauchy stress tensor **σ** with principal stress denoted as σ_I, σ_{II} and σ_{III} in the order of $\sigma_I \geq \sigma_{II} \geq \sigma_{III}$. The three stress invariants of the stress tensor are defined respectively by

$$I_1 = \sigma_I + \sigma_{II} + \sigma_{III}\ , \tag{2.1}$$

$$J_2 = \frac{1}{2}\boldsymbol{\sigma} : \boldsymbol{\sigma} = \frac{1}{6}\left[(\sigma_I - \sigma_{II})^2 + (\sigma_{II} - \sigma_{III})^2 + (\sigma_{III} - \sigma_I)^2\right]\ , \tag{2.2}$$

$$J_3 = \frac{1}{3}\mathbf{S} \cdot \mathbf{S} : \mathbf{S} = \det(\mathbf{S}) = (\sigma_I - \sigma_m)(\sigma_{II} - \sigma_m)(\sigma_{III} - \sigma_m)\ \ , \tag{2.3}$$

Where **S** is the deviatoric stress tensor and σ_m is the mean stress. The deviatoric stress is defined as **S**=**σ**+p**I**, where **I** is the unit tensor and p is the hydrostatic pressure. The deviatoric principal stress therefore has the order $S_I \geq S_{II} \geq S_{III}$. The mean stress, σ_m, and equivalent stress or von Mises stress, $\bar{\sigma}$, are defined as function of the invariants as:

$$\sigma_m = \frac{I_1}{3} \text{ and } \bar{\sigma} = \sqrt{3J_2} \tag{2.4}$$

The third deviatoric stress invariant J_3 can be normalized as

$$\xi = \frac{27}{2}\frac{J_3}{\bar{\sigma}^3} = \frac{3\sqrt{3}}{2}\frac{J_3}{J_2^{3/2}} \tag{2.5}$$

with $-1 \leq \xi \leq -1$, which characterizes the relationship between the intermediate principal stress, σ_{II}, and the major and minor principal stress, σ_I and σ_{III}. For any axisymmetric stress state, ξ equals to -1 or 1 for $\sigma_I = \sigma_{II} \geq \sigma_{III}$ and $\sigma_I \geq \sigma_{II} = \sigma_{III}$, respectively, and have a zero value when $\sigma_{II} = (\sigma_I + \sigma_{III}) / 2$.

In the present study, it is hypothesized that an accurate ductile fracture model should include the hydrostatic pressure (p), the stress triaxiality (η), and the Lode angle (θ), which can be expressed as:

$$\eta = \frac{\sigma_m}{\bar{\sigma}} \tag{2.6}$$

$$\theta = \frac{1}{3}\arccos\xi \tag{2.7}$$

The normalized Lode angle, named as Lode angle parameter, is written as follows, where $-1 \le \bar{\theta} \le 1$.

$$\bar{\theta} = 1 - \frac{6\theta}{\pi} = 1 - \frac{2}{\pi}\arccos\xi \tag{2.8}$$

2.2 New Ductile Fracture Criterion under Monotonic Loading

2.2.1 Stress Triaxiality Dependency

The stress triaxiality fracture dependency of ductile metals was first introduced by McClintock (1968), who studied the growth of long cylindrical voids under a prescribed history of applied principal components of stress and strain. Rice and Tracey (1969) proposed a similar exponential trend by evaluating the behavior of spherical voids in an incompressible, rigid-perfectly plastic solid for high triaxiality loading cases. The exponential function describing the effect of stress triaxiality on damage evolution of ductile fracture is shown in Equation 2.9 in terms of void growth rate

$$\frac{d\ln f}{d\bar{\varepsilon}} = c_1 \exp(c_2\eta) \tag{2.9}$$

where f is the porosity, $\bar{\varepsilon}$ is the equivalent plastic strain, c_1 and c_2 are material constants with $c_1 = 0.850$ and $c_2 = 1.5$ in the original work of Rice and Tracey (1969).

Johnson and Cook (1985) proposed an empirical and monotonic relation between the critical equivalent fracture strain and the stress triaxiality (for constant strain rate and temperature), expressed as

$$\bar{\varepsilon}_f = c_4 + c_5 \exp(c_6\eta) \tag{2.10}$$

where c_4 to c_6 are material constants and c_6 is postulated to be negative. When the stress triaxiality approaches positive infinity, the critical equivalent fracture strain tends to c_4. In such cases, the critical fracture strain is believed to be very small and can be assumed to equal zero. If the $\ln f$ term in Equation 3.12 is treated as a damage indicator with limit state value $D_c = 1$, the Rice-Tracy criterion can be transformed into Johnson-Cook criterion in Equation 2.10 under proportional loading condition using the mathematical operation in Equation 2.11, with $c_1 = c_5^{-1}$, $c_2 = -c_6$. Hence, the Johnson-Cook (J-C) and Rice-Tracy (R-T) criterion are actually identical to each other under proportional loading.

$$\frac{d\ln f}{d\bar{\varepsilon}} = c_1 \exp(c_2\eta) \;\Rightarrow \bar{\varepsilon}_f = c_1^{-1}\exp(-c_2\eta) \Rightarrow \bar{\varepsilon}_f = c_5 \exp(c_6\eta) \tag{2.11}$$

If c_6 is assumed constant with a value of -1.5 and η is set as a transient parameter, then Equation 2.11 reduces to the stress modified critical strain (SMCS) model. The Johnson-Cook model has gained its reputation in predicting tensile ductile fracture and has been widely embedded into commercial codes. However, it has been gradually losing its primacy in the literature for predicting ductile fracture since it is only a monotonic function of η and does not include the Lode angle effect.

From a mechanistic perspective, there are two main components that drive the void nucleation-growth-coalescence process: void dilation and shape/rotation. Under high triaxiality, exponential relationships can capture spherically symmetric volume-changes, the void dilation, because the dilation is driven by the hydrostatic stress components, which overwhelm the other shape-changing/rotation phenomenon caused by the deviatoric stress components. However, in cases with moderate or low stress triaxiality that will not introduce much dilation, the void shape-changing/rotation or other effects cannot be neglected; thus, stress triaxiality is no longer sufficient to predict the fracture locus. In the proposed model, it is assumed that the stress triaxiality dependency for the ductile fracture is described by the exponential formula in the Rice-Tracey and Johnson-Cook models.

2.2.2 Lode Angle Parameter Dependency

The Lode parameter effect on ductile fracture is relatively unexplored, and the physical mechanisms are not as clear as those associated with stress triaxiality. This kind of dependency may be due to changes in void shape or variation in growth direction. The importance of Lode parameter was first comprehensively evaluated experimentally by a series of tests (Bao, 2003; Bao and Wierzbicki, 2004; Wierzbicki et al., 2005b; Bai, 2008; Wilkins et al., 1980) and subsequently confirmed by Barsoum and Faleskog (2007), especially in the low and negative stress triaxiality range.

In the present study, damage owing to deviatoric stress, in terms of Lode parameter effect, is considered to constantly exist regardless of the stress triaxiality magnitude. In the high triaxiality range, it is relatively small compared with the damage from the hydrostatic stress, where tensile fracture dominates. In the negative stress triaxiality range, the roles of Lode parameter and stress triaxiality are opposite and shear fracture prevails. In the low stress triaxiality range, the two effects compete and neglecting either can lead to inaccurate estimates of damage and fracture strain. The effect of Lode parameter was considered to intermittently exist even in a negative stress triaxiality range in some studies (Xue, 2008; Nahshon and Hutchinson, 2008), which is different than what is assumed in this present study.

The Lode parameter dependency also received attention in the sheet metal forming industry where the main strain paths occur in the negative and low stress triaxiality ranges. Various criteria were proposed, including the maximum shear (MS) model, the modified Mohr-Coulomb fracture criterion (Bai and Wierzbicki, 2010), and many others. Wierzbicki et al. (2005a) evaluated the applicability of seven fracture models based on experimental results of 2024-T351 aluminum alloy, and surprisingly, the MS stress fracture model correlated well with the tests in low and negative triaxiality cases. However, the MS stress model failed to predict fracture in the high stress triaxiality range since the MS model does not include any stress triaxiality-related parameters. The MS criterion has been successfully used in the sheet forming process, which only involved a low and negative stress triaxiality range (Stoughton and Yoon, 2009).

Compared with the various models developed on ductile fractures in recent decades, the well-established MS criterion is found to be among the best predictors of ductile fracture in negative and low stress triaxiality ranges. Not only does it closely follow the trend of shear ductile fracture initiation and location, it also includes stable and generic damage parameters that allow its use for predicting failure of specimen with different geometry and similar forming conditions (Li, et al. 2011). From a mechanism perspective, the maximum shear stress is responsible for void shape change in the corresponding stage. In the final stage, two mechanisms were reported by Weck and Wilkinson (2008) and included necking of ligaments between voids and shear-linking of voids. The former usually occurs under high stress triaxiality and is due to maximum principal stress, while the latter mostly occurs in the low stress triaxiality range and is due to the maximum shear stress. Generally, the MS criterion may not necessarily out-perform other models in terms of accuracy, but it is overwhelmingly more economical and does not lag behind any of the other models. Therefore, the MS model is utilized to represent the Lode angle parameter in the proposed model.

2.2.3 Interaction of Stress State Parameters and New Ductile Fracture Criterion

The weighted sum method has been extensively applied to ductile fracture modeling that involves multiple factors, such as the modified Gurson model in Nahshon and Hutchinson (2008). Similarly, the weighted product method has been utilized, for example, in the Johnson-Cook model (Johnson and Cook, 1985), the X-W model (Xue and Wierzbicki, 2008), and the ductile fracture criteria in Lou et al. (2012). It is worth noting that these two methods are transformable and equivalent by performing logarithm arithmetic on both sides of the weighted product equation. In this section, the new criterion is derived using the weighted product approach.

The normalized MS criterion can be transformed into a function of $\bar{\theta}$, expressed as

$$\frac{\sigma_I - \sigma_{III}}{\bar{\sigma}} = \cos\left(\frac{\pi}{6}\bar{\theta}\right) \tag{2.12}$$

Since the equivalent fracture strain is highly dependent on both stress triaxiality and Lode angle parameter, and η and $\bar{\theta}$ are orthogonal to each other, the effects of the two variables are included in the unified fracture model but in a separable form in the present study. While the J-C/R-C and MS criteria are monotonic functions of η and $\bar{\theta}$, respectively, and are both well verified, it is reasonable to develop a fracture criterion for the whole stress triaxiality range that is based on both models. The new model can be written as

$$\bar{\varepsilon}_f = c_7 \exp(c_8\eta)\left[\cos\left(\frac{\pi}{6}\bar{\theta}\right)\right]^{c_9} \tag{2.13}$$

2.2.4 Damage Evolution Rule

Besides the previously discussed fracture locus as it relates to proportional and quasi-proportional loading conditions, the rule of damage evolution is critical for non-proportional loading cases. The damage evolution law is usually expressed in the format of an integral function of stress state, shown as

$$D = \int_0^{\bar{\varepsilon}_p} f(\eta, \bar{\theta})\, d\bar{\varepsilon}_p \tag{2.14}$$

in which the stress state parameters, $\eta(\bar{\varepsilon}_p)$, and $\bar{\theta}(\bar{\varepsilon}_p)$, are unique functions of the equivalent plastic strain. Since the ductile fracture criterion is described in terms of fracture strain, it is reasonable to define the relative loss of ductility of the material as the damage indicator, and Equation 2.14 can be transformed into

$$D = \int_0^{\bar{\varepsilon}_p} \frac{1}{\bar{\varepsilon}_f(\eta, \bar{\theta})}\, d\bar{\varepsilon}_p\,, \tag{2.15}$$

where $\bar{\varepsilon}_f(\eta, \bar{\theta})$ is defined by Equation 2.6 and Equation 2.8 at any point on the equivalent plastic strain excursion. The damage evolution rule has been adopted in many studies. When the damage indicator approaches one, that is $D(\bar{\varepsilon}_f) = D_c = 1$, the material element is considered to have failed.

The damage in Equation 2.15 is assumed to accumulate with a linear incremental dependence on the equivalent plastic strain, which has been widely used and shown to correspond well with monotonic loading conditions (Wierzbicki et al., 2005a; Bai, 2008). In the cases of reverse or other complicated loading paths, the linear dependency may not be valid, and a nonlinear incremental rule should be considered.

2.3 New Ductile Fracture Criterion under Reverse Loading

2.3.1 Description of the Stress State

In this section, two new parameters regarding the measure of the equivalent plastic strain, ε_p, which is a scalar, are employed in the fracture modeling. The first measure is the cumulative equivalent plastic strain $\bar{\varepsilon}_{pc}$, also named the effective plastic strain, and is defined by the rate form in Equation 2.16, while the second is the transient equivalent plastic strain $\bar{\varepsilon}_{pt}$ and is defined using Equation 2.17.

$$\dot{\bar{\varepsilon}}_{pc} = \sqrt{\frac{2}{3}\dot{\varepsilon}_p : \dot{\varepsilon}_p}\ . \tag{2.16}$$

$$\bar{\varepsilon}_{pt} = \sqrt{\frac{2}{3}\varepsilon_p : \varepsilon_p}\ . \tag{2.17}$$

Under monotonic loading conditions, since there is no direction change, the cumulative and transient equivalent plastic strains are equal and the relation $\bar{\varepsilon}_p = \bar{\varepsilon}_{pc} = \bar{\varepsilon}_{pt}$ holds. Under complex loading conditions involving significant load direction changes, however, the cumulative plastic strain is an ever-increasing scalar while its transient counterpart can decrease even under continuous plastic flow.

2.3.1 Extension of the Fracture Criterion from Monotonic Loading to Reverse Loading

Occurrence of fracture due to large reverse pre-crack straining, often termed as ULCF, falls in between the monotonic ductile fracture and traditional LCF fracture and shares more characteristics with monotonic loading-based fracture.

As previously stated, the direct extension from the monotonic fracture model to reverse loading through a linear damage evolution law provides inaccurate predictions. Hence, it is necessary to introduce modifications describing the “fatigue” influence on the linear damage incremental rule.

The damage in Equation 2.15 is postulated to accumulate in a linear fashion. The linear incremental relationship has been widely used in the literature (Wierzbicki et al., 2005a) for the quasi-proportional loading condition in which $\bar{\varepsilon}_f$ is treated as constant since the stress state parameters are assumed to be unchanged.

Perfect proportional loading is scarce in practical situations, and even under classical proportional loading η and $\bar{\theta}$ cannot remain unchanged in the final unstable stage near fracture. Therefore, linearity of the damage evolution is questionable in some sense. For the loading case without direction change, Bai (2008) indicated that the linear incremental rule was applicable after analyzing a series of experimental results. While this is questionable to some extent due to the mentioned changes in the stress parameters near fracture, it is understandable since no dramatic microstructural changes will take place in the absence of complex loading and stress reversals. It is important to emphasize, however, that the linear incremental rule is not applicable for complex or reverse loading conditions.

For the loading cases with directional change, namely reverse loading, employing the linear damage increment rule results in the D_c term at the limit $\bar{\varepsilon}_p = \bar{\varepsilon}_f$ being either increased and larger than unity, as in the case of 1045 steel as reported in Bai (2008), or reduced and smaller than one, as in the case for Al2024-T351 as reported in Bao and Treitler (2004). The discrepancy of fracture between the monotonic and reverse loading conditions has also been indicated through fractographic analysis, in which shallower dimples appear in the fracture surfaces in the case with reverse loading than the case under monotonic loading conditions (Kanvinde and Deierlein, 2007). Therefore, changes in loading direction play a role in damage evolution under reverse loading conditions.

It is postulated that the unconformity of damage indicators between the analytical and experimental results under complicated loading conditions may be caused by 1) the nonlinear nature of damage evolution, 2) the nonlinear influence of loading history defined by reverse loading, or 3) the combined effects of damage and loading history nonlinearities.

The linear ductility damage definition shown in Equation 2.15 is the simplest solution to Equation 2.14. Another straightforward solution with a more general format is shown as follows

$$D = \left(\frac{\bar{\varepsilon}_p}{\bar{\varepsilon}_f}\right)^m, dD = m\left(\frac{\bar{\varepsilon}_{pt}}{\bar{\varepsilon}_f}\right)^{m-1} \frac{d\bar{\varepsilon}_{pc}}{\bar{\varepsilon}_f} = mD^{\frac{m-1}{m}} \frac{d\bar{\varepsilon}_{pc}}{\bar{\varepsilon}_f}, \tag{2.18}$$

where m is a material constant.

The history effects of existing plastic strain excursions on subsequent damage evolution were addressed by Bao and Treitler (2004) and Kanvinde and Deierlein (2007) by assuming that the effects depend on the accumulated equivalent plastic strain in the form of continuous and cyclic stepwise magnification of the damage accumulation function. However, plastic strain exists regardless of the non-proportionality during any kind of loading process and therefore cannot be viewed as the source of the history effects in reverse loading.

It is assumed in the present study that the immense deviation from proportional loading during the reverse loading process is the main source of the history effects on the damage evolution. A new parameter is introduced to describe the effects on the following damage evolution from the previous non-proportional loading history, expressed as

$$\kappa = \int_0^{\bar{\varepsilon}_{pc}} \beta d\bar{\varepsilon}_{pc}, \tag{2.19}$$

where β is defined as

$$\beta = \frac{\sum_{i=1}^{3}\sum_{j=1}^{3}\sigma_{ij}}{\|\boldsymbol{\sigma}\|_1} - \frac{\sum_{i=1}^{3}\sum_{j=1}^{3}\alpha_{ij}}{\|\boldsymbol{\alpha}\|_1}, \tag{2.20}$$

where $\boldsymbol{\alpha}$ is the back stress tensor. The parameter β is designed to describe the stress state non-proportionality, featured with a range of [-2, 2].

It is postulated that the non-proportionality of the loading history affects the damage evolution law in Equation 2.14 in the following format

$$dD = \exp\left(c_{14}\kappa\right)\frac{d\bar{\varepsilon}_p}{\bar{\varepsilon}_f(\eta, \bar{\theta})}, \tag{2.21}$$

where c_{14} behaves as a weighing parameter requiring calibration and represents the effect of non-proportionality on accelerating damage evolution when $c_{14}\kappa > 0$, decelerating damage when $c_{14}\kappa < 0$, and no non-proportionality effects when $c_{14}\kappa = 0$. When under proportional loading conditions with $\kappa = 0$, Equation 2.21 will reduce to Equation 2.15. It is noteworthy that in the first half cycle the two equations provide the same damage increments. As discussed before, plastic strain occurring at the cut-off regions speeds up or retards subsequent damage evolutions. It is also worth pointing out that the integral boundaries of Equation 2.19 cover the whole range of the plastic strain paths, even in the cut-off regions.

The history effects correspond to LCF cases with negative stress ratio, $R = \sigma_{\min}/\sigma_{\max} < 0$, as well as the possible phenomena of fatigue crack closure. During crack closure and the simultaneous compressive load, the crack surfaces are highly compressed, resulting in crack sharpening and subsequent acceleration of crack growth. However, it is noted that not all the compressive load is used to collapse the voids and sharpen the crack tip. Instead, some and perhaps most of the compressive load is dissipated during the process of reversing the residual stresses from the preceding tensile cycle in the vicinity of the crack tip, resulting in a subsequent decelerated crack growth. As previously stated, the acceleration and deceleration effects are described in Equation 2.21 by $c_{14}\kappa > 0$ and $c_{14}\kappa < 0$, respectively. If the stress ratio is always positive, such history effects should be eliminated.

Since the effects of the nonlinear increment and loading history are defined in Equation 2.17 and Equation 2.21, a damage evolution in the format of Equation 2.21 is proposed under the assumption that the two effects behave independently and simultaneously.

$$dD = \exp\left(c_{14}\kappa\right) m \left(\frac{\bar{\varepsilon}_p}{\bar{\varepsilon}_f}\right)^{m-1} \frac{d\bar{\varepsilon}_p}{\bar{\varepsilon}_f(\eta, \bar{\theta})} \tag{2.22}$$

It should be noted that the values of m and c_{14}, calibrated using Equation 2.19 and 2.21, respectively, may not be applicable to Equation 2.22, and new parameters have to be determined based solely on Equation 2.22.

2.4 Concluding Remarks

Fracture after few reverse loading cycles, or ULCF, is one of the predominant limit states in metal structures subjected to extreme loading cases. Based on past research, the underlying mechanisms for ULCF are presumed to be similar to the ductile fracture mechanisms under monotonic loading conditions. Ductile fracture has been proven sensitive to two-stress state parameters, namely the stress triaxiality and Lode angle parameters. Thus, the fracture criterion developed with dependency on both the stress triaxiality and Lode angle parameter, is extended for reverse loading cases. Worthy of note is the intrinsic difference between the reverse and monotonic loading condition; mainly, the extent of variations of the stress state parameters, the fracture cut-off region, as well as the nonlinearity and history effect on damage evolution make the direct extension of the fracture model from monotonic to reverse loading inapplicable.

Unlike monotonic loading conditions, the load path under ULCF can result in stress state parameters that fall outside the boundaries of the cut-off region. As previously discussed, this has been proven to exist in many experimental studies.

The extension from monotonic to reverse loading conditions was achieved by the development of an appropriate ductility-based damage evolution law. The linear damage incremental rule has been confirmed to be only applicable to monotonic/quasi-proportional loading conditions, and the difference between the empirical and analytical prediction results when linear damage evolution is utilized is postulated to be due to two parts, namely the nonlinear nature of the

damage evolution law and the influence of the loading history. The two parts are modeled and embedded into the ductility-based damage incremental rule in both a separate and a combined format.

3. VALIDATION AND IMPLEMETATION OF THE NEW FRACTURE MODEL TO STRUCTURAL DETAILS WITH BLOCK SHEAR FAILURE

3.1 Introduction

Block shear is one of the governing failure modes for bolted connections. In a block shear failure, a block of material is partially or entirely torn out from the parent component. The most significant feature of block shear is the presence of varying stress state conditions that cause the fracture to propagate on a tension and shear plane and, in some cases, with additional inclined planes. The presence of these different failure paths undoubtedly will have an impact on the resulting connection strength and ductility. Therefore, the ability to model such failure can provide very useful information on the true behavior of the connection. It is important to note that simulations conducted in previous studies, due to limitations in modeling capabilities, were unable to capture failure of the connection (i.e., no crack initiation or propagation). This is because capturing such failure requires the utilization of a fracture model that allows for the development of tension and shear failures in the connection. In other words, a unified ductile fracture model that is applicable to a wide range of stress triaxiality and Lode parameter is required for proper predictions.

The most representative block shear fractures are usually associated with gusset plate and coped beam connections. In gusset plate connections, the development of block shear is due to direct tension loading on a member connected to the gusset plate. There have been many laboratory tests on gusset plate connections, and accurate and reliable data have been obtained from these tests (Whitmore, 1952; Hardash and Bjorhovde, 1984; Bjorhovde and Chakrabarti, 1985; Nast et al., 1999; Huns et al., 2002; and many others). However, tests that included the entire fracture process up to and including failure, with focus on the fracture mechanism, are relatively limited. In coped beam connections, the development of block shear is a result of pure shear loading at the connection that could be coupled with the second moment carried by the connection because of beam rotation. Compared with gusset plate connections, bolted coped beams are featured with asymmetric stress distribution resulting from the complex loading conditions. As a result, the failure path is also often asymmetrical, and thus existing gusset plate failure tests cannot directly be extended to the bolted coped beam connections. Block shear failure in coped beams was first identified by Birkemoe and Gilmor (1978) through comparative testing that included one coped and one un-coped beam, and subsequently confirmed through testing conducted by Yura et al. (1982), Ricles and Yura (1983), and Aalberg and Larsen (2000). Franchuk et al. (2002) conducted 17 full-scale tests on coped beams with bolted double angle connections in order to evaluate the influence of multiple variables related to geometry and loading conditions on failure. Fang et al. (2013) and Lam et al. (2015) also conducted several groups of tests in order to investigate the effect of single angle bolted and double bolt-line on the behavior and failure of the connections.

Due to the high cost and limitations associated with full-scale tests, numerical simulation can serve as a substitute or supplement to testing and can provide meaningful insight on complex phenomena. Numerical simulation on connections pertaining to block shear evolved from the two-dimensional linear elastic and nonlinear finite element models (Ricles and Yura, 1983; Huns et al., 2002; Franchuk et al., 2002; Wen and Mahmoud, 2015a) to three-dimensional solid element nonlinear models (Yam et al., 2007; Wei et al., 2010; Yam et al., 2011; Fang et al., 2013). The previous studies provided viable predictions of connection strength in some cases but not in others. In addition, limitations in modeling capabilities did not allow for the development and propagation of cracks, which are essential to include for reliable predictions of connection capacity and ductility.

In this section, numerical simulations on block shear in gusset plate and coped beam connections are conducted up to and including total failure through the application of a newly developed ductile fracture criterion with consideration of both the stress triaxiality and Lode angle parameter. The laboratory test results from Huns et al. (2002) and Franchuk et al. (2002) are utilized for validation of the numerical modeling approach and for comparing the outcome of the numerical study to real experimental data and observations. The comparisons include load versus displacement curves, fracture sequence, and fracture profile. Through the numerical simulations, the inherent mechanisms of block shear in gusset plate and coped beam connections, including the effect of various levels of beam end rotations on connection behavior, are thoroughly discussed. Next, a parametric study is conducted with a focus on geometrical variables, which include bolt spacing in the tensile and shear planes and bolt edge/end distances. Through the parametric study, four different fracture modes are identified and analyzed for the first time, and contradictions between the numerically obtained predictions and those predicted using the design equations are found and shown, which indicates the need for further design code modification.

3.2 Gusset Plate Connection

3.2.1 Description of Laboratory Tests

There are many experimental programs on gusset plate connections, the majority of which terminated soon after fracture initiation; hence, lacking information on fracture propagation. Laboratory tests on gusset plate connections up to and including failure, however, were conducted by Huns et al. (2002), and therefore are ideal candidates for validating the numerical models. Two configurations, named T1 and T2, which were loaded up to total failure in tension, are chosen for the validation. A simple sketch of the two test setups is shown in Figure 3.1. The displacement, Δ, in Figure 3.1 was monitored along the centerlines of the connections, which, together with the loading force, F, were used to generate the load-displacement curve of the connection. More details of the experimental setup, including photos of the fracture profiles and specimen configurations, can be found in Huns et al. (2002).

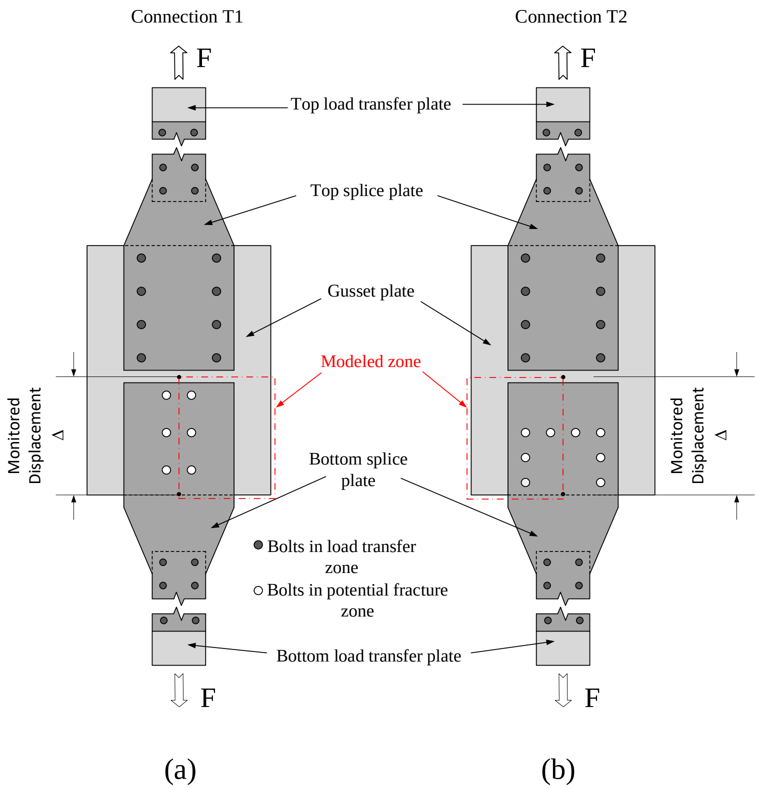

Figure 3.1 Tests set up for gusset plate connections: Specimen (a) T1, and (2) T2, *after Huns et al., 2002*

3.2.2 Description of Numerical Modeling

The general finite element (FE) program ABAQUS/Explicit (Simulia, 2012) was employed in the present numerical simulations. Since both gusset plate connections, against which the simulations will be compared, showed minute to no out-of-plane deformations during the entire test, two-dimensional plane stress elements, CPS4R, were employed in the simulations. A refined mesh size with 1×1 mm resolution was used at and around the fracture zones. Taking advantage of symmetry, only half of the specimen was modeled to reduce the computational time as marked by the “modeled zone” with a large dashed box in Figure 3.1. Nonlinear material behavior was introduced through the isotropic hardening model embedded in ABAQUS, and the material parameters are adopted based on the corresponding coupon tests in Huns et al. (2002). Since the experimental program was designed for investigating fracture in the gusset plate, the bolts were designed with large safety factors where only minor deformation would occur in all bolts. Therefore, the bolts in this study were modeled as rigid bodies. The load in the analysis was simulated through displacements of the bolts. A friction coefficient of 0.3, representing Class C slip factor for untreated hot rolled steel per the 2010 AISC Specifications (AISC LRFD, 2010), was used primarily to introduce the bolt-plate interaction. The upper boundary conditions were modeled as fixed, where there are only insignificant stress/strain fields. A typical numerical model of a gusset plate is shown in Figure 3.2 for specimen T2.

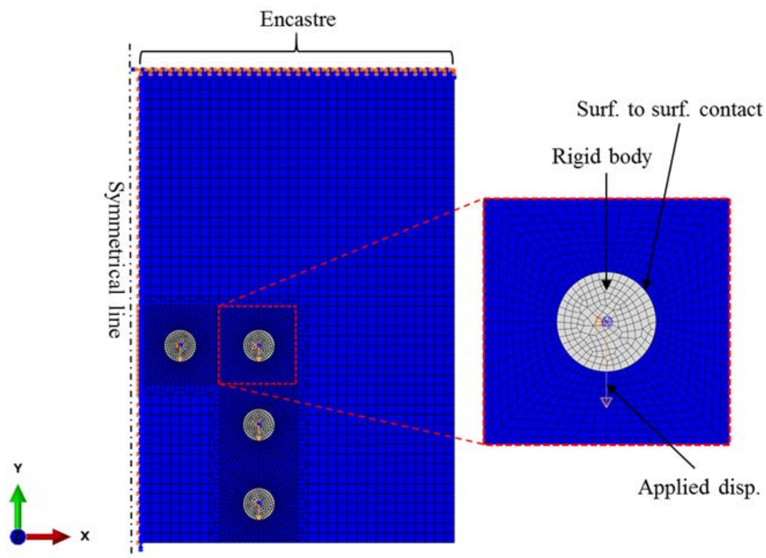

Figure 3.2 Numerical model for gusset plate connection T2

Calibration of the parameters of the fracture model was conducted through trial and error, and an in-house study on similar steel calibrated in Wen and Mahmoud (2016a). After obtaining the calibration values of the parameters, the fracture criterion in Equation 3.18 becomes as follows,

$$\bar{\varepsilon}_f = 0.7506\exp(-1.9232\eta)\left[\cos\left(\frac{\pi}{6}\bar{\theta}\right)\right]^{-3.3546} \tag{3.1}$$

3.2.3 Simulation Results of Gusset Plate Connections

Comparisons between the numerical and experimental final fracture profiles are shown in Figure 3.3 (a) and (b) for specimen T1 and T2, respectively. As shown in the two figures, the simulated fracture profiles correlate exceptionally well with their experimental equivalents. The fracture sequences were also simulated with a high level of accuracy for both specimen T1 and T2, and the comparison for the sequences between the numerical and experimental is shown in Figure 3.4 for specimen T2, as an example, which comprises 1) horizontal tensile necking, 2) horizontal tensile fracture and shear yielding, and 3) vertical shear fracture. At the final fracture propagation stage, the residual strength shown in the load versus displacement curves in Figure 3.5 (a) and (b), for models T1 and T2, respectively, results from the shear plane, which continued to provide strength following the fracture of the tension plane until complete fracture. Very strong correlation is also observed between the experimental and numerical load versus displacement curves, as shown in Figure 3.5 (a) and (b) for connection T1 and T2, respectively, which can be attributed to the high level of accuracy in simulating the fracture sequence. It is important to note that fracture was introduced in the models through element deletion once the damage in Equation 2.15 reaches the critical value 1.

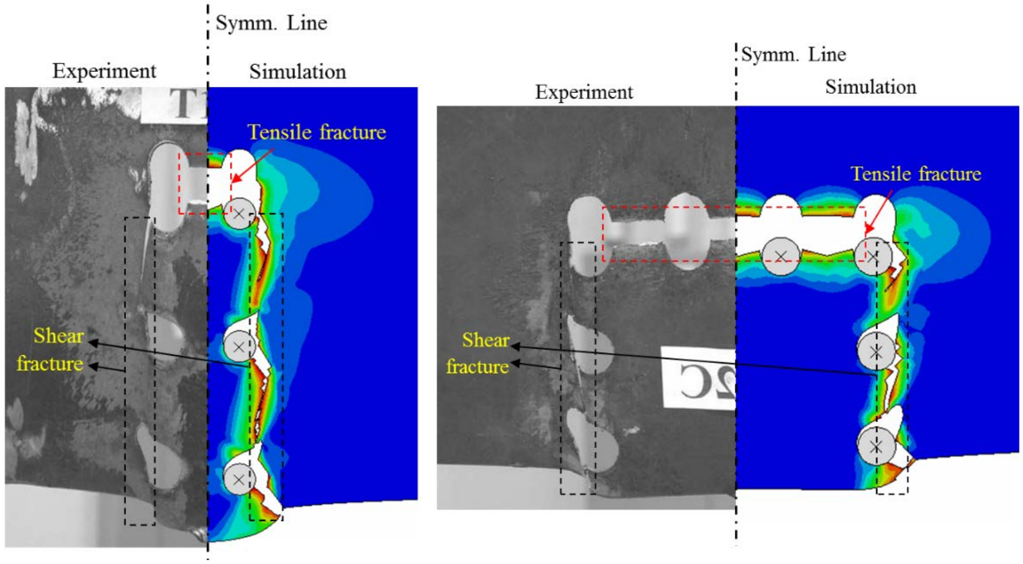

Figure 3.3 Comparison between the experimental and numerical fracture profiles of connection (a) T1 and (b) T2

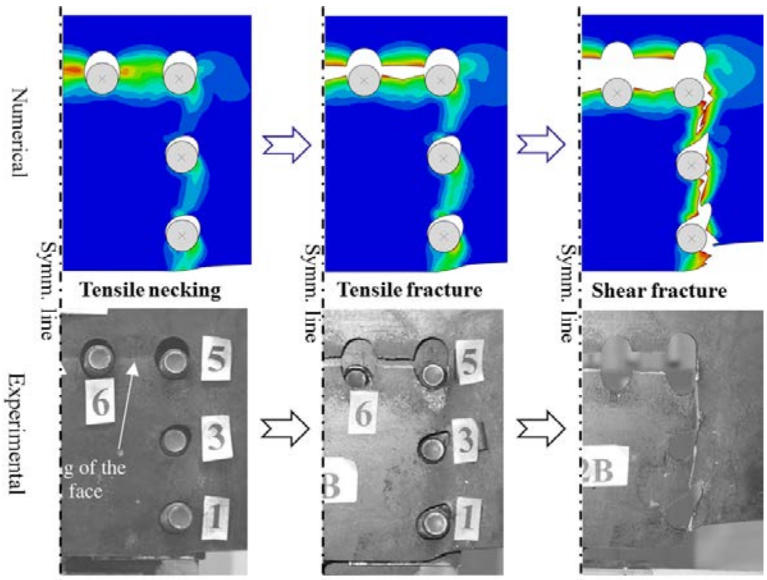

Figure 3.4 Fracture sequence of the connection T2

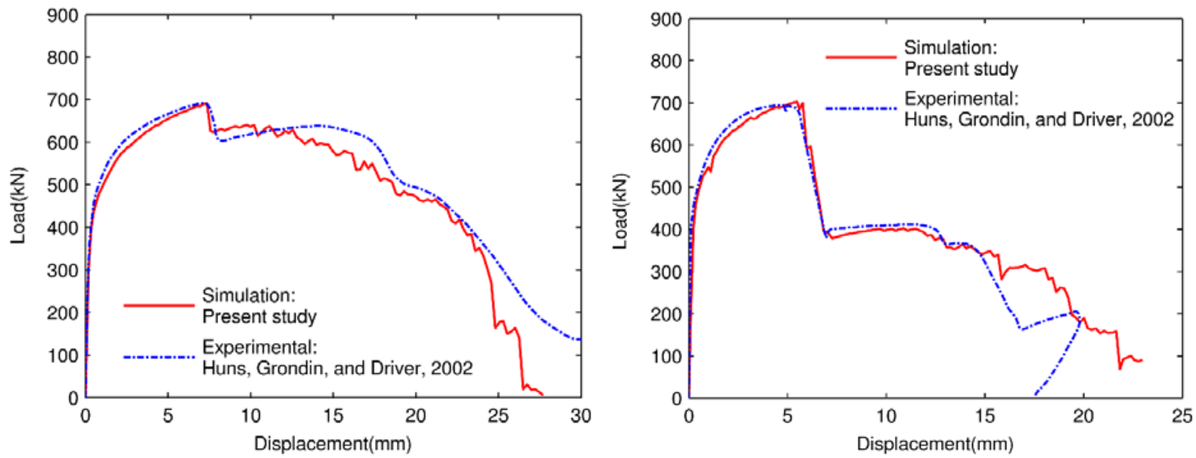

(a) (b)

Figure 3.5 Numerical and experimental load versus displacement curve of connection (a) T1 and (b) T2

3.3 Coped Beam Connection

3.3.1 Description of Laboratory Tests

There are 17 full-scale tests conducted on coped beams with bolted double angle connections in Franchuk et al. (2002), among which two specimens were fabricated using W310×60 and the remaining 15 were fabricated using W410×46. Each beam was coped at both ends. There were nine beams designated with letters A through J, excluding I, and each two connections on the same beam were named by a number 1 or 2. A representative sketch of the tested beams is shown in Figure 3.6 (a). Three of the 15 specimens, designated C2, J1 and J2, had a two-line bolt configuration, while the others had only one line of bolts. Discrepancy was shown for the tested specimens with two lines of bolts with significant disagreement in the results between specimens with same configurations. The specimen A1 indicated local buckling during the loading, and reconfigured for reloading, so it is not adopted for simulation in the present study. Therefore, in the present study, for the sake of calibrating the models and predicting the behavior using consistent experimental data, only the 11 specimens with a single-line bolt, fabricated from W410×46, are considered as the comparative cases.

There were two groups of specimens (A2, B1, B2 and F1, H1, H2), where the specimens in each group shared the same geometry but underwent different beam end rotations. Other specimens (C1, D1, D2, E1, E2) were featured with unique geometries and were subjected to zero end rotations. All in all, there were seven different connection geometries, and three levels of end rotations for all beams involved, categorized in Table 3.1 and illustrated in Figure 3.6 (b) and (c). The different levels of end rotations were achieved by controlling the displacement, Δ3, with linear increment, while imposing load stroke Δ4. For maintaining zero end rotations, Δ2 was kept at zero. More details regarding the experimental set up and procedures can be found in Franchuk et al. (2002).

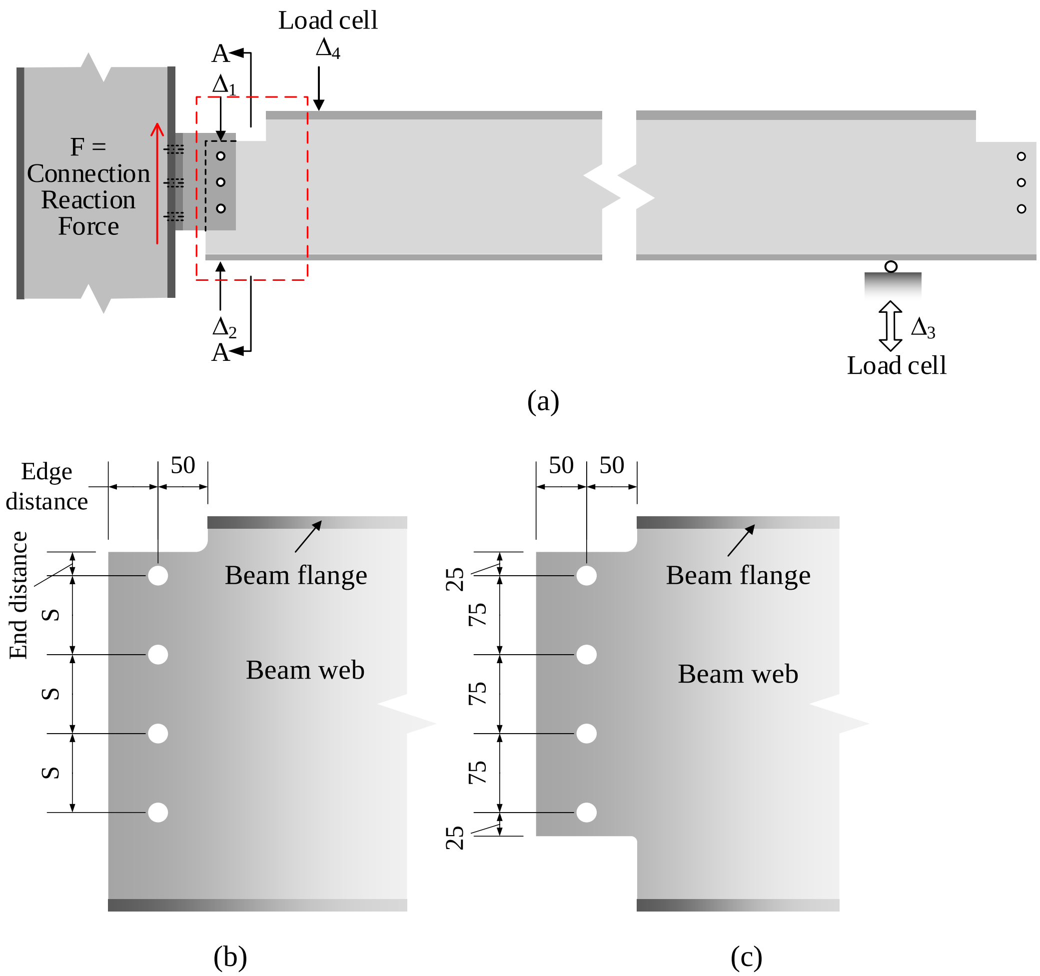

Figure 3.6 (a) Representative beam geometry and set up, (b) representative geometry of connections subjected to end rotation, and c) Geometry of connection of specimen D2 subjected to zero end rotation (i.e., pure shear)

The block shear deformation, Δ, which equals the difference between Δ_1 and Δ_2 on the beam in Figure 3.6 (a), was taken as the displacement indicator in the load versus displacement behavior, and the calculated connection reaction force, F in Figure 3.6 (a), was used as the load indicator.

Table 3.1 Geometries for all the specimens

Connection designation	Edge distance (mm)	End distance (mm)	Spacing (S) (mm)	Rotation (degrees)	Number of bolts
A1	25	25	75	0	4
A2				3.5	
B1				2	
B2				0	
C1	25	25	102	0	3
D1	32	32	103	0	3
E1	50	25	75	0	4
E2	25	50	75	0	4
F1	25	25	75	0	3
H1				2	
H2				3.5	

Note: Since the pure shear specimen D2 is featured with distinct geometry, it is shown in Figure 3.6 (c) separately instead of in Table 3.1.

3.3.2 Description of Numerical Modeling

Similar to the gusset plate models, the general finite element platform ABAQUS/Explicit was also employed in the simulations. Out-of-plane deformations were not observed for almost all beams during the entire phase of testing, and consequently no buckling failure modes were identified. Therefore, the two dimensional plane stress elements, CPS4R, were utilized in the simulations for the sake of computational efficiency. Finite element models for selected beams were first developed then validated through extensive comparisons with the corresponding experimental results. The comparisons included load versus displacement curves as well as fracture profiles. The mesh size employed in the coped beam simulations was 3mm×3mm, at and around the fracture region, and is outlined with the dash line and the corresponding zoom in as shown in Figure 3.7.

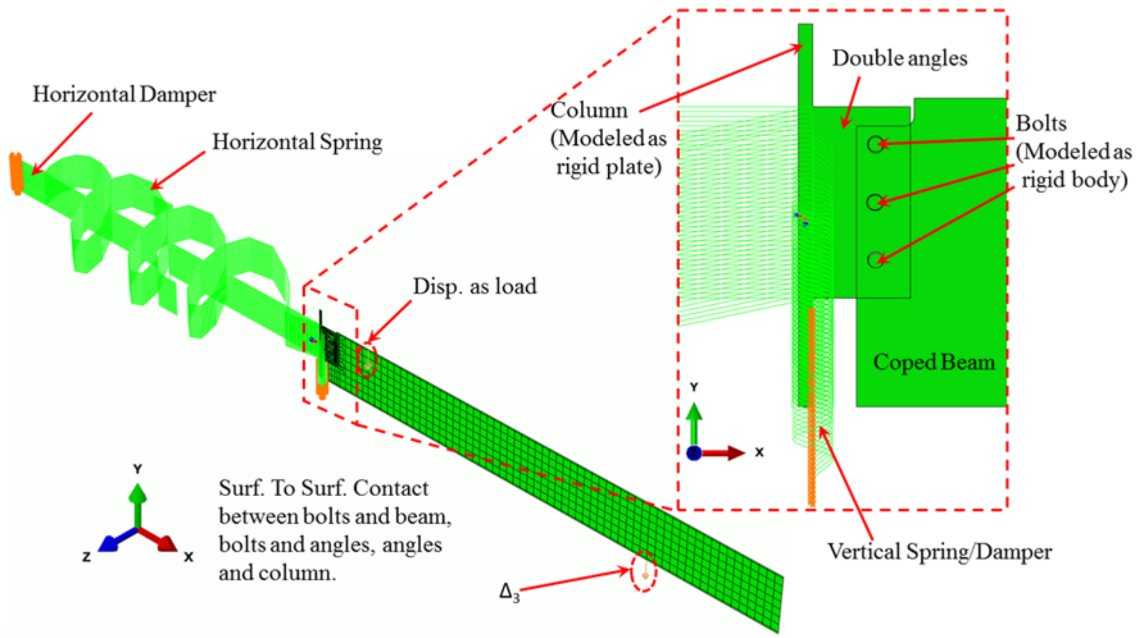

Figure 3.7 Representative numerical model for coped beam connection

An isotropic hardening material model embedded in ABAQUS was adopted in the numerical analysis, with the data extracted from coupons taken from the webs of the respective beams. A friction coefficient of 0.3, representing Class C slip factor for untreated hot roll steel per the 2010 AISC Specifications (AISC 360-10), was used primarily to introduce the bolt-hole interaction. Because the experimental program was designed to investigate the fracture of the beam, the bolts were designed with large safety factors. Since no obvious deformations were observed from bolts and columns, the bolts were modeled as rigid bodies, and their ignored stiffness was small and can be offset through boundary conditions that incorporate springs with appropriate coefficients, as will be discussed in the following section. Bolt preload was not considered in the FE simulations since the bolts were only snug-tightened in the corresponding laboratory programs.

Boundary conditions, representing load and support conditions, in the corresponding laboratory tests were considerately modeled in order to mimic the testing protocol. In the laboratory tests, the beam was loaded slowly under displacement control. Most of the tests were designed without applied end rotations, and the supporting jack [Δ_3 in Figure 3.6 (a)] was adjusted but in very small increments (±0.25 mm), so it can be viewed as a pin in these cases. For the tests with end rotations, the jack was lowered at each load increment to achieve the desired rotations, which are in a linear relationship with the vertical reaction and calculated through the predicted ultimate strength and desired ultimate rotation. The numerical models developed in this study follow exactly the experimental procedures for the application of the load and modification of the support conditions. The displacement was incremented through a specified displacement of the node in the top flange corresponding to Δ_4 and the corresponding force measured. The displacement, Δ_3, was also specified at a node on the bottom flange.

Two sets of vertical and horizontal spring elements were applied to simulate the vertical and horizontal constraints from the bolts between the double angles and columns. The corresponding stiffness, modeled through spring elements as discussed in the following section, from the constraints consists in reality of several resistances, including resistance to slippage between the angles and columns, local bearing deformation of every bolt hole, as well as local deformation of the bolts. In addition, a set of dampers was also applied along with these spring elements in order to dissipate the dynamic response from the fracture phenomena. The forces from the dampers are minute compared with those induced by the springs and therefore are neglected during calibration. A representative setup for the spring system and dampers is shown in Figure 3.7 (a), and details of the methodology by which the spring coefficients are calculated is introduced in the following section. As in the case of the gusset plate models, the fracture behavior in the FE model was captured through the implementation of the fracture criterion in Section 2 and achieved through element deletion.

3.3.3 Calibration of FE Model

The series of vertical and horizontal springs served as a substitution for the constraints between the double angles and columns. There are many factors influencing the vertical and horizontal stiffness of the connection system. This includes, for example, bearing on bolt hole both the vertical and horizontal directions, bolts' bending and elongating, angles' bending away from column (horizontal bending) and vertical bending, slippage in every bolt in each direction and many other localized deformations. Most of these nonlinear and complex features are difficult to precisely measure and account for even if full details of the connections modeled are available. Therefore, some simplifications are applied.

In the present study, the vertical stiffness system is decomposed into two parts: the global stiffness, K_g, representing the mean stiffness components of the entire bolt line, and the local stiffness, K_l, representing the stiffness components unique to each individual bolt. The stiffness contributions from the behavior of friction between the column flange and double angles, angles' bending action, and other local deformations from the columns and angles are assumed to affect only the global stiffness performance.

The local stiffness, on the other hand, is assumed to be only influenced by bolts bearing on the angles and column holes (angles to column flange connections), since the stiffness from bolts bending is relatively small. The local springs are all connected in parallel and are in series with the global springs. A prototype spring system layout is shown in Figure 3.8, and the overall stiffness, K, combining the local and global springs, can be determined through Equation 3.2.

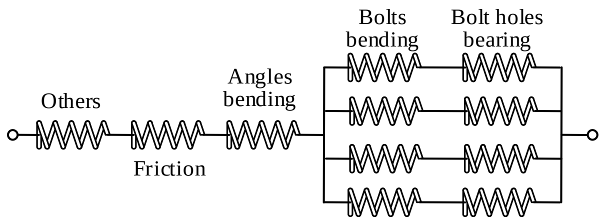

Figure 3.8 Spring system layout for vertical spring

$$K = \frac{1}{1/K_g + 1/(3K_l)} \quad \text{or} \quad K = \frac{1}{1/K_g + 1/(4K_l)} \tag{3.2}$$

The stiffness of bolt bearing on plates, K_l, in the present study can be determined by Equation 3.3 as outlined in Rex and Easterling (2003), as follows

$$K_l = \frac{1}{1/K_{br} + 1/K_b + 1/K_v}, \tag{3.3}$$

where K_{br} = bearing stiffness, K_b = bending stiffness, and K_v = shearing stiffness. The three sub-stiffnesses are calculated by Equation 3.4 to 3.6 (Rex and Easterling, 2003), expressed respectively as

$$K_{br} = 120 t_p F_y (d_b/25.4)^{0.8}, \tag{3.4}$$

$$K_b = 32 E t_p (L_e/d_b - 1/2)^3, \tag{3.5}$$

$$K_v = 6.67 G t_p (L_e/d_b - 1/2), \tag{3.6}$$

where t_p is the plate thickness, d_b is the bolt diameter, F_y is the yield stress, E is the modulus of elasticity, G is the shear modulus of elasticity, and L_e is the end distance, which represents the length between the center of bolt and nearest end edge in the anticipated direction of loading.

The global stiffness can be determined through Equation 3.7. The angles' bending action can be simplified to a two-end fixed beam with concentrated force in the mid-span, as shown in Figure 3.9, and the corresponding stiffness $K_{AngleBending}$ can be determined from Equation 3.8. The other two components in Equation 3.7 are treated together as one term, and usually assumed to be featured with infinite starting value in the following trial and error.

$$K_g = \frac{1}{1/K_{AngleBending} + 1/K_{friction} + 1/K_{others}} \tag{3.7}$$

$$K_{ab} = 192 EI / L^3 \tag{3.8}$$

The 11 tested specimens of interest are featured with seven different geometries, and for each of the seven geometries a test with zero end rotation was conducted. The presence of zero rotation provides a convenient way to measure the entire stiffness of the connection in the vertical direction. As shown in Figure 3.10, when the ultimate load is achieved, the beam end rotation is approximately zero, which implies that the connection in the beam end has shifted downward and the horizontal stiffness of the system has no influence on the load versus displacement curve. A trial and error method was employed to calibrate the global stiffness, K_g, by correlating the beam end rotation to the load versus displacement curves, with K_g in Equation 3.7 serving as a starting point. The adjustment to K_g is rather insignificant for all beams, implying that the starting point in Equation 4.7 is quite adequate.

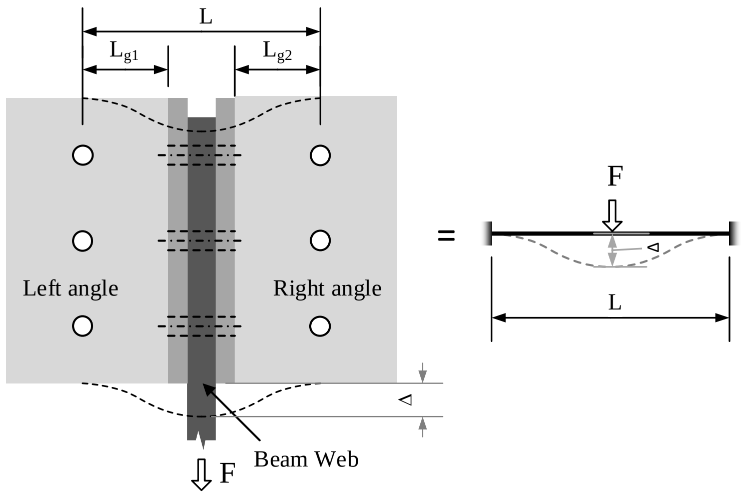

Figure 3.9 The two-fixed end beam system for the angles' bending action [A-A section of Figure 3.6 (a)]

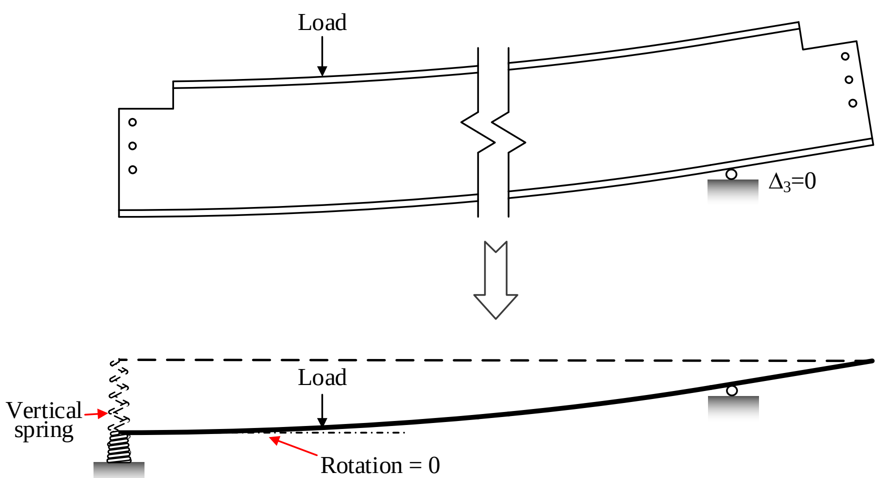

Figure 3.10 Layout of the calibration on global systems through zero rotations

In cases where the beam end rotation exits, the stiffness in the horizontal direction should be considered, as shown in Figure 3.11. Unlike the bolts' performance in the vertical direction, the orientations of bolt bearing on the angles are not the same, and there is no obvious global stiffness, K_g, which leads to the local stiffness, K_l, dominating the overall stiffness. The end rotations cause the upper bolts to move away from the column while the bottom bolts are pushed toward the column. For the bottom bolts, only K_{br} is present in Equation 3.7 since the angles are tied with the column because of the compression. Except for the stiffness contribution from the bolt bearings on the angles, the actions of angles' bending away also influence the behavior of upper bolts. In the laboratory tests, a 12.7-mm-thick cover plate was attached to reduce the bending of the angles away from the column, and no information was provided to describe the cover plate detail; hence, it is not possible to account for the cover plate effect. Therefore, the lateral stiffness of the bolts was primarily determined by the bolt bearing stiffness model, expressed in Equation 3.6. In addition, reduction in the stiffness, determined from trial and error, was applied to the stiffness of upper bolts, which accounts for the effects from angles' bending away (horizontal bending) and other possible local actions in the systems. During calibration of the models, the initial location of bolts inside the bolt hole showed noticeable but not significant influence on the initial stiffness of the load versus displacement curves and fracture profiles, which will be discussed in the following sections.

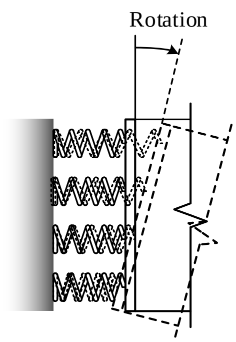

Figure 3.11 The sketch of the horizontal spring system

3.3.4 Calibration of Fracture Criterion

There are three parameters that require calibration in Equation 2.15, and each holds unique influence on the fracture locus map. The parameter c_7, as a positive value, only proportionally varies the magnitude of the fracture strain. The parameter c_8 relates to the dependency of stress triaxiality, and c_9 pertains to the Lode angle parameter sensitivity to the criterion. The unique role of each of the three parameters greatly reduces the effort required for calibration. In the original experimental tests of the coped beams, the fracture strains were not measured since they were not of interest. Fortunately, a previous in-house study on a coupon level has narrowed the value of c_8 to approximately -1.9. One of the seven geometries previously mentioned connection D2 in Figure 3.6 (c) was designed to be fractured under pure shear stress state ($\eta = \overline{\theta} = 0$) and was used to determine c_7. Very good agreements between the simulation and the experiment is achieved under c_8= 0.5 in the perspective of load versus displacement behavior and fracture profile. The remaining parameter, c_9, was obtained through trial and error on specimen B2 so that the best correlation between the experimental and numerical results for the load versus displacement curve and fracture profile is obtained. The resulting three fracture parameters in Equation 2.15 for this steel type, for the 15 tested beams, are c_7=0.5, c_8=-1.9, and c_9=-6.2. Once the three parameters were obtained, they were utilized for predicting the response of all remaining specimens.

3.3.5 Simulation Results of Coped Beam Connections

The numerical simulation procedure is verified by comparisons between the numerical and experimental results, specifically in terms of the load versus displacement behavior fracture profiles. The loads and displacements were calculated from the numerical models using the same procedure as that of the experimental study. The displacements are the difference between the top displacement, Δ_1, and bottom displacement, Δ_2, along the bolt lines, and the loads are the supporting forces from the columns, which are designated as the reaction force F in Figure 3.6(a). The load versus displacement curves for specimens with zero rotations are reviewed, and the representative ones are plotted in Figure 3.12 (a) through (e). Very good correlation is observed for all the beams with zero rotations, not only before cracking occurred but also after fracture has initiated. For the cases with large beam end rotations, such as H2, in the fracture progression stage, the agreements between the analytical and experimental curves are questionable, although the trends are still well predicted, as shown in Figure 3.12(f). The reason for the lack of accurate predictions beyond the capacity point is due to the large rotation that causes a very complex stress distribution, which results in a multifaceted failure path, as discussed later. For beam D2 in Figure 3.12(d), the plateau in the early increase stage may be due to the slip of the bolts, and the numerical simulation successfully simulated this phenomenon by including the bolts' slippage.

The final fracture profiles are shown in Figure 3.13 for the representative analysis cases as well as their experimental equivalents. It is shown that all the fracture profiles produced numerically correlate very well with the corresponding ones obtained from the tests. The tensile fracture on the horizontal plane and shear fracture on the vertical plane work together to form the entire tear-out, which is a key feature of block shear failure. It is noted that most of the cases present a clear block shear fracture, but for the ones with large beam end rotations, such as H2, the fracture profile on the shear plane shows tearing along a complex path that started away from the bottom bolt hole. No information on the fracture sequence is available in Franchuk et al. (2002). The fracture sequence, obtained numerically, for the loading cases without beam end rotations, the fracture mostly initiates as a tensile fracture at the outer horizontal plane of the bottom bolt. In the cases with rotations, however, the fracture initiation transfers to the bottom bolt in the vertical direction as shear fracture.

For specimens with end rotations, the specimens were designed to experimentally undergo three levels of rotations: 0°, 2°, and 3.5°. Because of the complexity in measuring these rotations, the actual experimentally achieved end rotations were different, as shown in Table 3.2. Comparisons of the forces and end rotations at ultimate load between the numerical and experimental results are listed at Table 3.2. As shown in the table, very good correlation is observed.

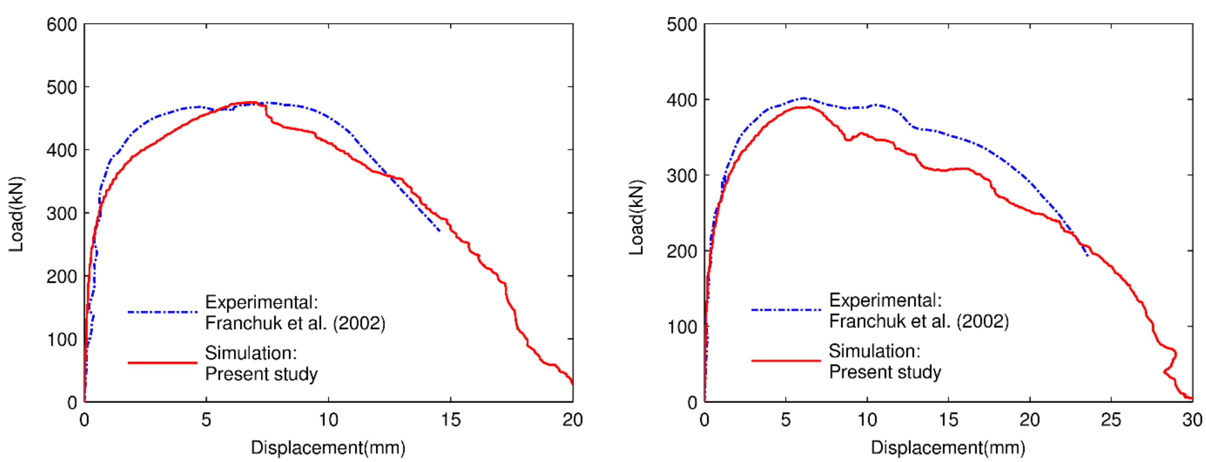

(a) (b)

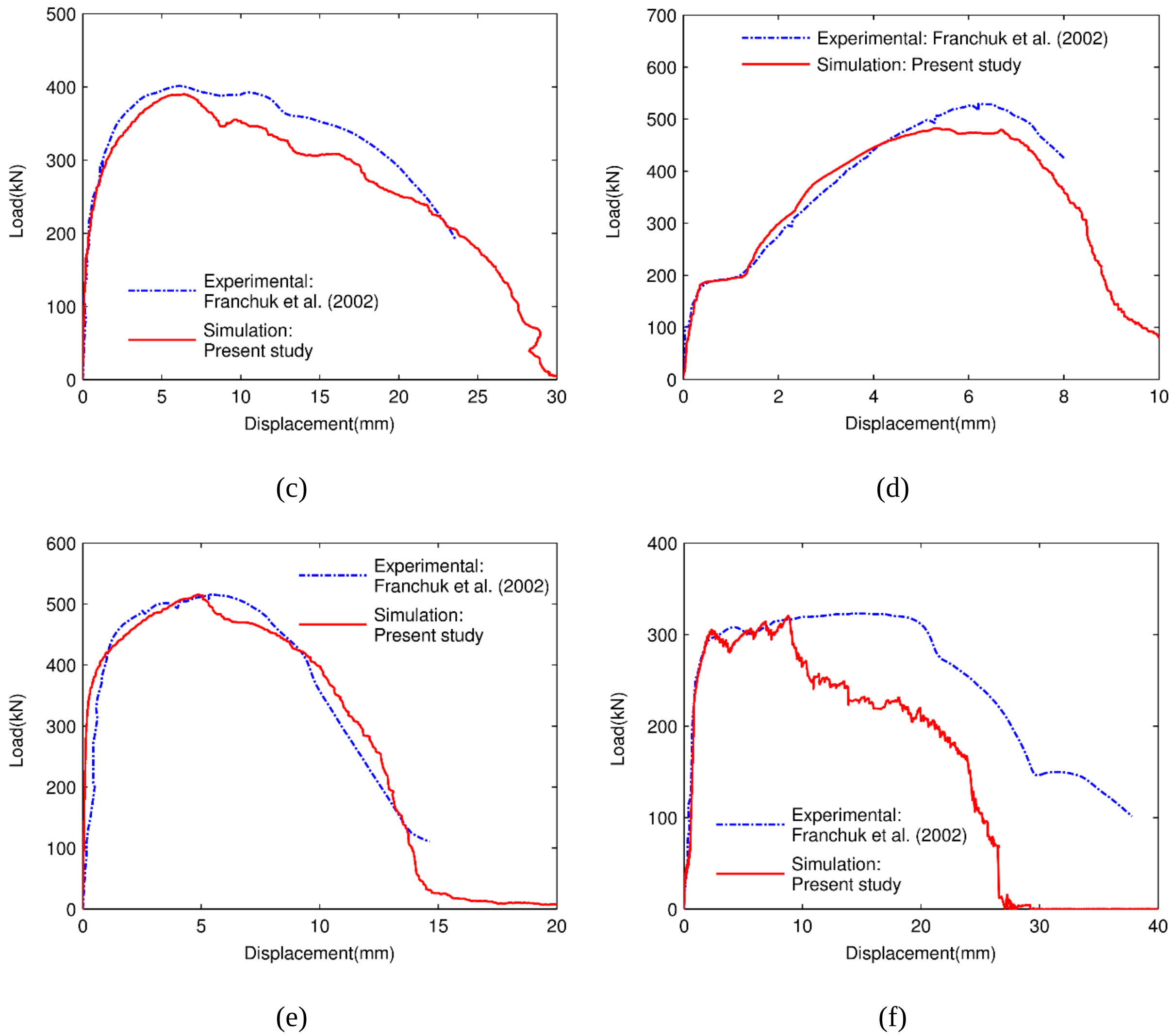

Figure 3.12 Representative comparisons between the numerical and experimental load versus displacement curves for (a) specimen B2, (b) specimen C1, (c) specimen D1, (d) specimen D2, (e) specimen E2, and (f) specimen H2

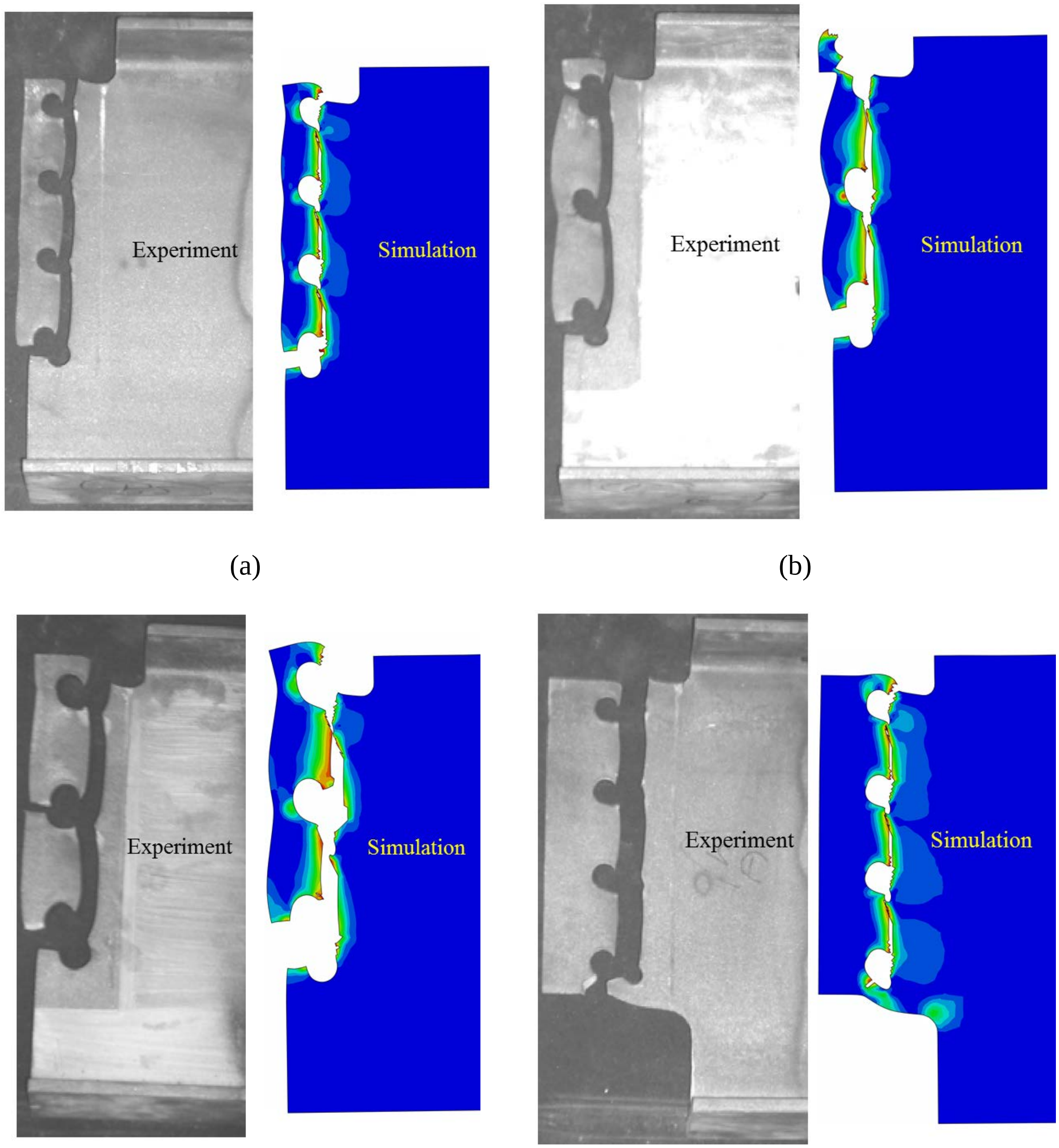
Experiment
Simulation
Experiment
Simulation
Experiment
Simulation
Experiment
Simulation

(a) (b) (c) (d)

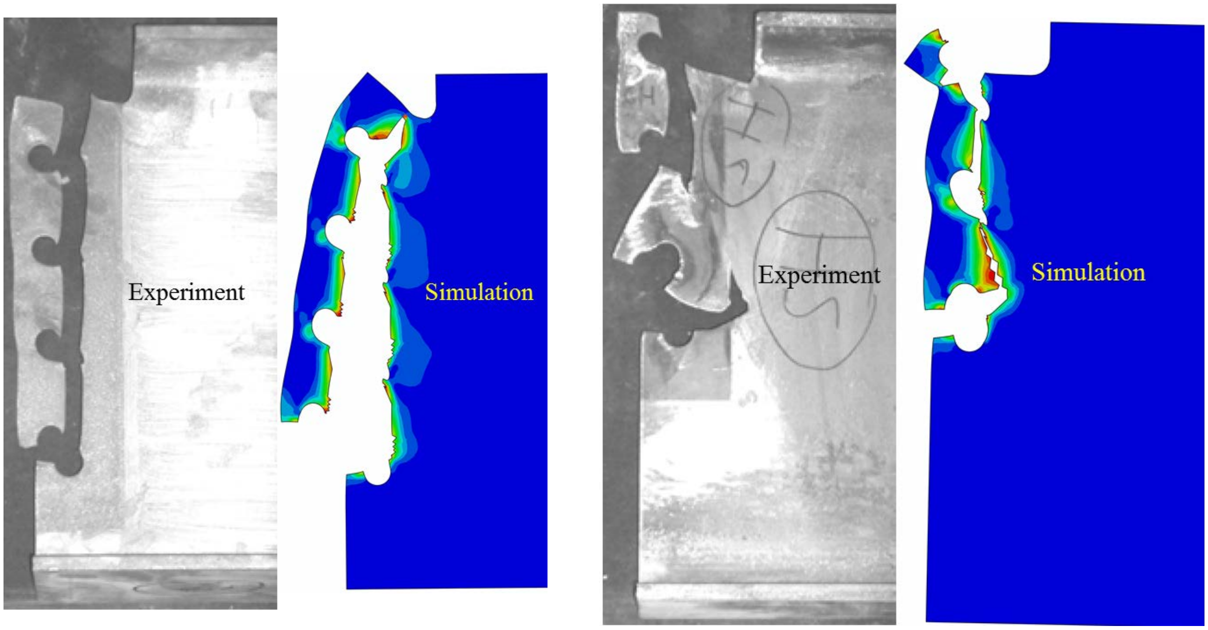

(e) (f)

Figure 3.13 Experimental and numerical fracture profiles for (a) specimen B2, (b) specimen C1, (c) specimen D1, (d) specimen D2, (e) specimen E2, and (f) specimen H2

Table 3.2 Comparisons of forces and beam end rotations for connections at ultimate load [Experimental data from Franchuk et al. (2002)]

Connection #	Peak Exp.vertical reaction (kN)	Peak Num. vertical reaction (kN)	Exp. End Rotation (°)	Num. End Rotation (°)	Force Error (%)
F1	324	338	-0.1	0	4.32%
H1	324	319	1.6	2.0	-1.54%
H2	341	318	3.2	3.5	-6.74%
A2	496	473	3.3	3.5	-4.64%
B1	514	474	2.0	2.0	-7.78%
B2	475	475	0.1	0	0.00%
C1	402	390	0.2	0	-2.99%
D1	448	459	0.2	0	2.46%
D2	529	483	1.9	0	-8.70%
E1	568	565	1.1	0	-0.53%
E2	517	515	0.5	0	-0.39%

3.4 Discussion on Block Shear Mechanism

There are many factors influencing strength and ductility under block shear in bolted connections, such as the geometry, loading conditions, and load sequence. In addition, these factors will have an impact on fracture path and sequence, which should be well understood so as to allow for the development of accurate design provisions that can encompass the proper failure modes.

3.4.1 Fracture Initiation Location on the Shear Plane

In this section, the mechanism of the fracture initiation sequence and fracture path in bolted connections is explained through extensive analysis of the gusset plate connection, T2. The reason for choosing specimen T2 is because of the simplicity in the applied loading and boundary conditions for the gusset plates in comparison with the coped beams such that the fracture path is not influenced by any anomalies. In Figure 3.14 (a) and (b), contours of the stress triaxiality and Lode angle parameter, for T2, prior to fracture are plotted, respectively. Figure 3.14(b) shows the Lode angle parameters are close to zero, and if the dependency of Lode angle parameter is ignored, such as in the Rice-Tracey criterion in Equation 2.12, the fracture strain will be overestimated, resulting in non-conservative predictions of strength and delay of fractures. The fracture strain contour, defined by Equation 3.18, for the same bolt arrangement is depicted in Figure 3.15. Generally, the stress triaxialities on the horizontal tension plane are higher than the ones on the shear vertical plane and, as a result, the tension plane is featured with smaller fracture strain, as shown in Figure 3.15. Hence, the tension fracture usually occurs first, but if there is high-localized shear strain field in the shear plane, shear fracture also may occur prior to tensile fracture.

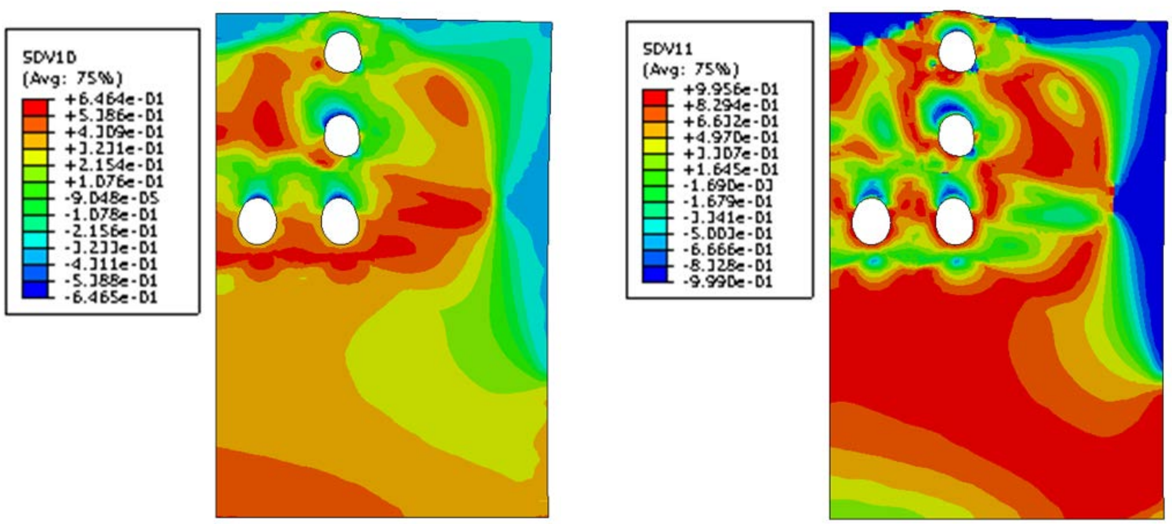

(a) (b)

Figure 3.14 Contour of stress state parameters for specimen T2: (a) stress triaxiality and (b) lode angle parameter

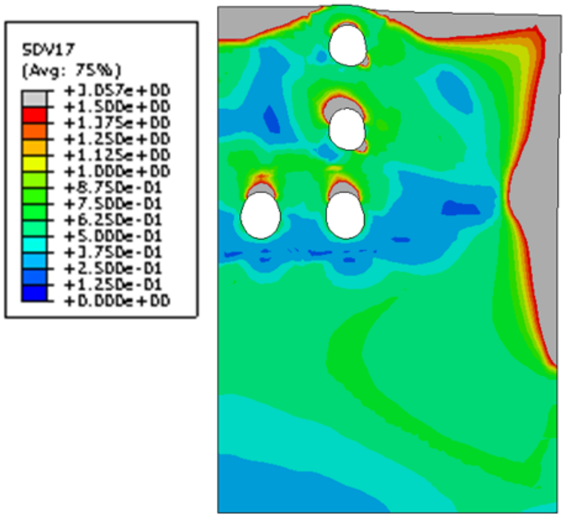

Figure 3.15 Fracture strain contour of T2

The damage contour directly prior to cracking is depicted in Figure 3.16 (a), and all four bolts are numbered. As previously discussed, for specimen T2, the damage is more significant on the tensile plane while on the shear plane some moderate damage has accumulated, implying yielding on the shear plane. The damage evolution before cracking corresponds well with the design equations in the 2010 AISC Specification (AISC 360-10) in that the total capacity of the connection equals the sum of the ultimate strength of the tensile plane and the yield strength of the shear plane. The load versus displacement curve is shown in Figure 3.16 (b) and is marked with numbers at different points along the curve. The designation, n_1, refers to the first crack on bolt hole, n, while n2 refers to the second crack on the same bolt hole. The fracture sequence can be defined on the load versus displacement curve where crack 1_1 occurs first on the inner side of the hole, then immediately crack 1_2 starts on the outer side of the hole and soon propagates to bolt hole 2, crack 2_1. After the entire tensile fracture is formed, the first shear crack that forms is 4_1, then 4_2 forms. Thereafter, crack 2_2 develops and the last cracks are 3_1 and 3_2.

Another parameter that can shed light on the fracture path is the damage distribution on the edge of each bolt hole, where specific points along the bolt hole edge can be defined by the angle from the horizontal axis, as depicted in Figure 3.17. The damage is plotted along the bolt hole edge for bolt 1 to 4, as shown in Figure 3.18 (a) to (d), respectively. As shown in Figure 3.18 (a), damage on bolt hole 1 reaches a value of one at approximately 0° and 180°, which implies failure on the net tension area as expected. The second hole, participating on the tension and shear planes, shows a damage value of one at approximately 180° on the tension plane and at 67.5°, not on the net section at 90°, for the shear plane. For holes 3 and 4 on the shear plane, the damage reaches a value of one at approximately 270° (center of bottom edge of the hole), which together with a damage value of one at 67.5° at the top edge of the hole form slanted cracks on the shear plane. The slanted fracture lines can also be observed in the laboratory tests, as shown in Figure 3.13.

The observation made above for the shear fracture not being along the centerline of the bolt holes, which has the least area, but rather at some locations between the gross and net sections, has been made by others. This phenomenon has been loosely accounted for in some codes (AISC, 1999; CSA-S16-09) where the shear strength is calculated using the gross plane rather the net plane. There is no clear explanation in the literature on the reason for the fracture shift on the shear plane. In this study, this phenomenon can be explained using the ductile fracture model in Equation 3.18. Specifically, due to the interactive compressive action between the bolt and bolt holes, negative stress triaxialities exist on the plate adjacent to the compressed bolt hole, shown in Figure 3.14 (a), which may result in very high fracture strain, even higher than that of the cut-off region, which is clearly shown in Figure 3.18. The damage can barely accumulate in these locations, which is clearly shown in Figure 3.18 for the bolt hole edges at around 90°. Thus, fracture cannot occur along the centerlines of the bolt holes, and usually detours to take place between the net and gross shear areas. On the other hand, there is no compressive action on the lower side of the bolt hole, such that the fracture usually tends to go back to the centerlines of the holes, seeking least resistance through least area, resulting in a slightly slanted fracture profile on the shear plane.

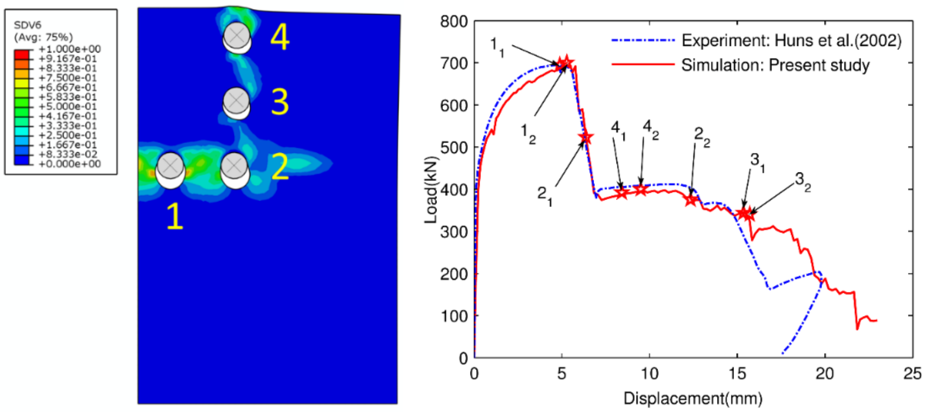

Figure 3.16 (a) Damage contour for connection T2 directly before cracking occurs and (b) sequence of fracture initiations on bolt holes

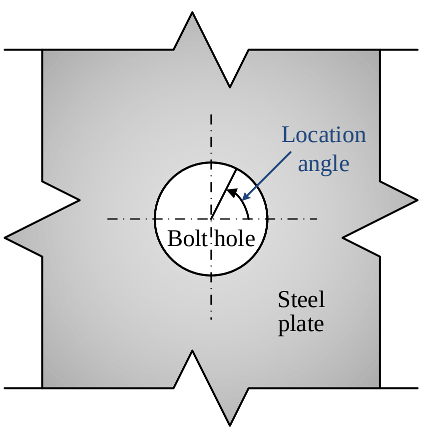

Figure 3.17 Definition of the location angle in bolt hole

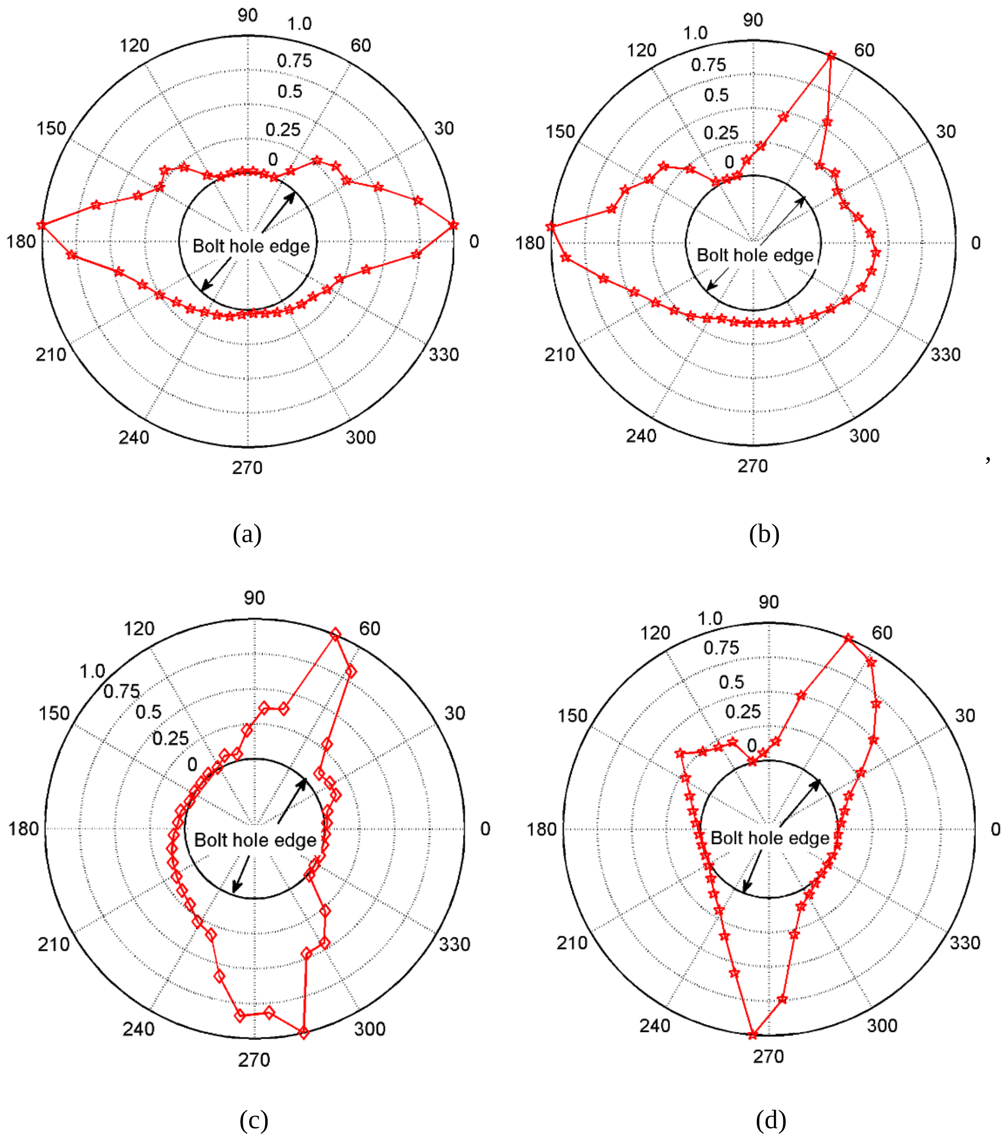

Figure 3.18 Depiction of damage distribution around bolt holes for (a) bolt hole 1, (b) bolt hole 2, (c) bolt hole 3, and (d) bolt hole 4.

3.4.2 Effect of Loading Conditions on the Connections

Research regarding the effect of loading conditions, specifically the moments/rotations, on coped beams, is scarce. Through the experimental results, Franchuk et al. (2002) concluded that moments/rotations did not hold adverse influences on the ultimate strength, but the failure modes might be transferred from normal block shear, such as F1, to partial block shear, such as the H1. However, no attempts were made toward understanding the intrinsic mechanism of failure resulting from end moments/rotations. In this section, the effect of beam end moment/rotations is explored through the advantage of numerical simulations.

In the validation section, two groups of specimens, F1 and H1 and A1, A2, B1, and B2, share the same configurations, but were subjected to different levels of beam end rotations. Specimens A1, A2, B1, and

B2 did not show significant differences although the end rotations were distinct. Specimens F1 and H1 showed many different performance features, and therefore can serve for exploring the objective in this section. Specifically, F1 was loaded without beam end rotations while H1 was subjected to large rotation (3.2° at the onset of fracture). The responses in the pre-fracture stage for the two cases are very close, but after fracture initiation, their behaviors show considerable differences. To better understand the effect of beam end rotations on the behavior of coped beam connections, several other specimens are numerically analyzed. The configurations of the new specimens are the same as that of F1 and H1, while the beam end rotations vary from 0° to 3.2°. The loading case numbers, the corresponding rotation levels, and the resulting sequence of fracture initiation are shown in Table 3.3.

Table 3.3 Rotations and fracture initiations of different load cases

Load case #	Rotation	Fracture initiation
a	0	T
b	0.5	T/S
c	1.25	S
d	2	S
e	3.2	S

T: tension fracture first; S: shear fracture first;
T/S: simultaneous tension & shear fracture

The final fracture profiles of all load cases are shown in Figure 3.19. The figure shows that an increase in beam end rotation results in more irregularity in the fracture profiles on the shear plane with significantly more tearing on the inner side of the bottom bolt hole. Additional tension fracture occurs on the outer side of the top bolt hole under large rotation levels. When the rotation levels become larger, the fracture initiation transfers from tensile fracture on the bottom bolt hole to the shear fracture on the top bolt hole.

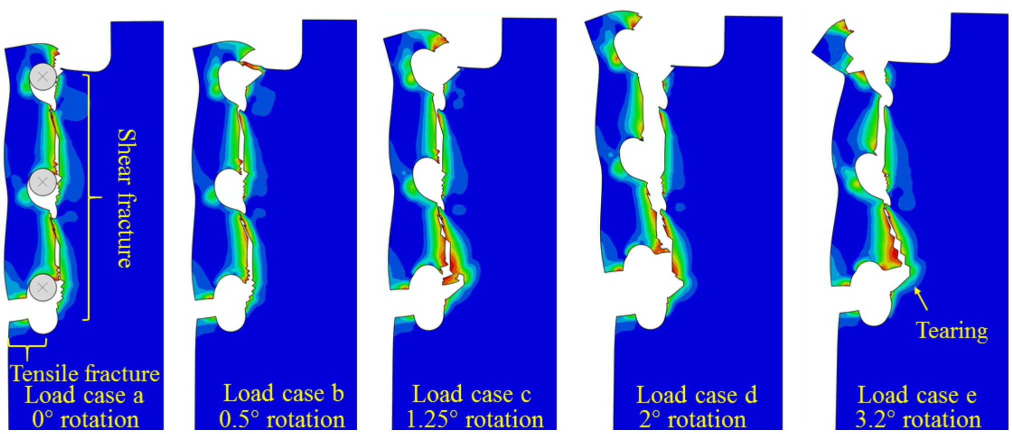

Figure 3.19 Comparisons of fracture profiles under different beam end rotation levels

The load versus displacement curves are close in the pre-crack stage for all the specimens, as shown in Figure 3.20, with a slight increase in the initial stiffness as the rotation increases. The strength obtained in all load cases is somewhat similar, with a minor reduction in the increase of rotation levels. Although minor, the decrease in the strength conflicts with the experimental results in Franchuk et al. (2002). The disagreement is however understandable since many factors could influence the experimental results, such as friction between the beam and double angles, the lateral support, and the material variation. In the fracture propagation stage, the higher the rotation level the more additional ductility is present.

The anomalies in the fracture profiles and sequences, as influenced by end rotations, can be explained by the bolt-hole interaction forces in the horizontal direction, shown in Figure 3.20. The figure shows that with growth of rotation levels, the horizontal bolt-hole interaction forces for the bottom and top bolts increase, and then these forces are transferred to the plate around corresponding bolt holes. For the top bolts, the forces are toward the beam end directions and subsequently tear the outer parts of beam end out of the beams. Hence, there are additional tension fractures on the top bolt for load cases with large rotation, shown in Figure 3.20, and the fracture initiates in the form of combined shear and tension fracture. For the bottom bolts, the forces compress the inner sides of bolt holes and accordingly decrease the stress triaxiality in the corresponding area. As discussed in the previous section, smaller stress triaxialities bring higher fracture strains and slower damage rates, and consequently fracture initiation detours to the locations easier to crack, which are usually below the compression zone and include relatively smaller fracture strains. In addition, with the increasing bottom compression forces, there might be slight local buckling in the inner side of the bolt hole, which may introduce extra ductility to the system and be the reason for the relatively inaccurate simulation in Figure 3.13 (f).

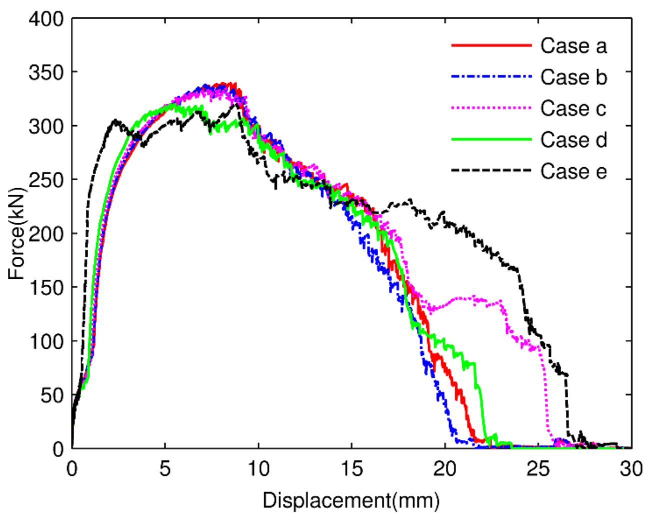

Figure 3.20 Comparisons of load versus displacement curves under different beam end rotation levels

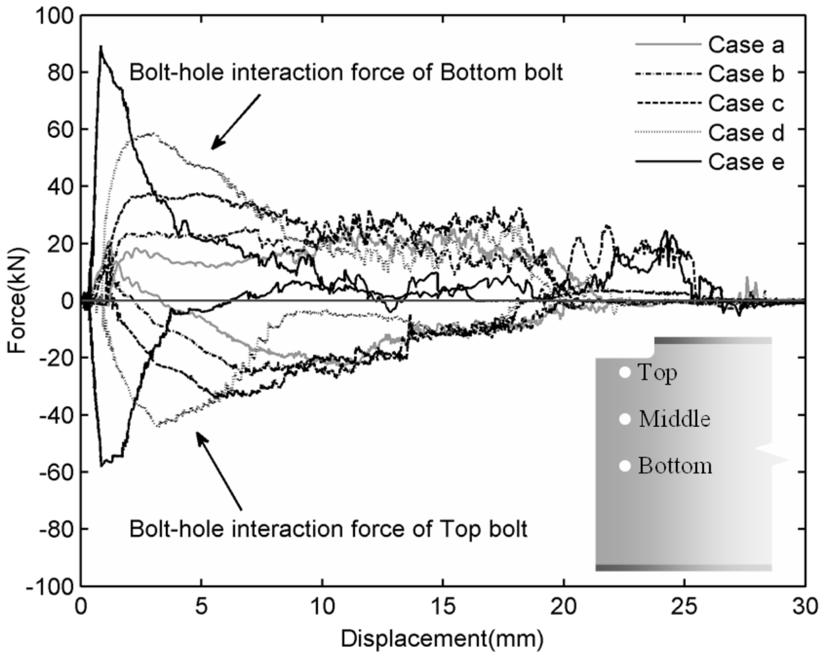

Figure 3.21 Comparisons on the bolt-hole interaction forces for top and bottom bolts under different beam end rotations

3.5 Conclusive Remarks

In this section, numerical simulations on block shear in gusset plate and coped beam connections were conducted up to and including total failure through the application of newly developed ductile fracture criterion. The laboratory test results from Huns et al. (2002) and Franchuk et al. (2002) served as validations of the numerical simulation approach for the gusset plate and coped beam connections, respectively. The numerical simulation results correlated well with the corresponding experimental equivalents for the load versus displacement curves, fracture sequence, and fracture profiles. After the numerical methodology was implemented and the ductile fracture criterion employed, the inherent mechanisms of block shear in gusset plate and coped beam connections were discussed and explained. The behavior of the coped beam connections with various levels of beam end/rotations was also explored.

Based on the simulations and analysis, the following conclusions can be drawn:

1. Based on the excellent agreements between the numerical and experimental results, the numerical modeling methodology and employed ductile fracture criterion are proven to be a viable approach for simulating block shear failure in bolted connections.
2. For tensile fracture, the fracture usually initiates and propagates on the net section, which confirms the approach used in current code specifications in that the net section is where tensile fracture takes place.
3. For shear fracture, the fracture paths were identified to be located between the net and gross sections, slightly larger than the net section.

The beam end rotation levels appear to have some minor effect on the strength of the connections, but the most significant influence lies on effect of such on ductility and fracture profile of the connections. The end rotations can greatly change the fracture profile and sequence where the top bolt holes become the holes most prone to fracture instead of the bottom bolt holes. It is also shown that the assumption of zero rotation levels may not be adequate if applied to cases with large rotations.

4. VALIDATION AND IMPLEMETATION OF THE NEW FRACTURE MODEL TO STRUCTURAL DETAILS UNDER CYCLIC LOADING

4.1 Introduction

Many natural and man-made hazards, such as earthquakes, strong winds, fatigue, and blast loading, will lead to cyclic stress/straining on critical structural details and subsequent failures. There have been many studies on the response of steel structures under elastic and small inelastic cyclic loadings, and the corresponding predictions of such through numerical simulations are widely confirmed and well developed since they usually do not require simulation of fracture. In cases where large inelastic demand is expected, usually a prescriptive target performance is assigned to mark the onset of connection failure without actually simulating fracture. The proposed ductile fracture model under cyclic loading in section 2 provides a viable approach to simulate the entire fracture process. In this section, the proposed ductile fracture model under reverse loading is also verified on the structural details level, through comparison between numerical simulations of shear links that are typically employed in EBFs and their experimental equivalents. The good comparisons also further validate the developed fracture model and the modeling approach for predicting the entire response of steel connections and buildings under any large inelastic cyclic deformations. The simulated specimens are selected from a group of shear link experimental tests conducted by Gálvez (2004), since sufficient information was provided in those laboratory tests regarding the entire response of all specimens up to entire failure.

4.2 Shear Links

4.2.1 Description of Laboratory Tests

An experimental program, whose test setup is shown in Figure 4.1, was conducted at the University of Texas at Austin (Arce, 2002; Gálvez, 2004; Okazaki, 2006) in order to reproduce the loading and displacement environment on a link in an EBF with one end of the link attached to a column. As shown in Figure 4.2 (a) and (b), the link specimens were fabricated through welding heavy end plates at each end of the W section, while the end plates were bolted into the column and beam in the experimental setup. All sections were fabricated using ASTM A992 steel, and the material properties were obtained through tensile coupon tests taken from flanges and webs of the specimens. The material tests were conducted for only some of the specimens, which were not similar since it was stated they were supplied by different manufacturers. In addition, only the stress-strain response of the coupon tests was provided. The main purpose of utilizing these coupon tests in this study is for calibration of the basic material properties, including the modulus, yield and fracture stress, and the hardening behavior parameters. Therefore, the damage and hardening parameters for a similar steel grade, ASTM A572 Grade 50, were used as the initial parameters in the following analysis; however, it should be noted that different specimens may be featured with different yielding stresses.

There were nine specimens tested with different geometries or loading conditions in Gálvez (2004), seven with stiffeners welded to link web, and two with stiffeners that only "touch" the link web. The main objective of this section is to explore the implementation of the newly proposed criterion in Chapter 2, and hence only three specimens are simulated, including the two without welding, and another one with welding. The importance of including a welded specimen lies in the fact that the effect of welding heat on the base metal's fracture properties has been shown in previous studies to be significant but never quantitatively investigated. The specimen without stiffener-web welding are featured with the same geometries but subjected to different loading protocols, denoted as specimen 1, whose geometry configurations are shown in Figure 4.2 (a), and this specimen corresponds to specimens 5 and 8 in Gálvez (2004), which have the same configurations but different loading protocol. The configuration of another specimen with stiffener-web welding is shown in Figure 4.2 (b), and is denoted as specimen 2, corresponding to specimens 1, 2, and 3 in Gálvez (2004), which are featured with the same geometry configurations but from different manufacturers. There are two loading protocols adopted, in which the first protocol is named revised loading protocol (RLP) used for specimen 1 and shown in Figure 4.3 (a), and the other is called the severe loading protocol (SLP) used for specimen 2 and shown in Figure 4.3 (b). It is noted that a zone on the web adjacent to the flange, named as "k-area," is featured with different material properties with other parts of the web. The material in the "k-area" has higher ultimate strength and smaller ductility, but the difference is quite unstable, depending on the manufacturers. Despite the difference, distribution of the "k-area" is very limited, only within around a 25-mm range from the flange, and although it has been proven as not the primary source of the fracture initiation in web (Okazaki and Engelhardt, 2007), it may have some effects on the fracture propagation. Therefore, a constant fracture resistance reduction factor of 0.8 is assumed for the "k-area," which means the parameters in Equation 2.22, except c_7, are assumed to hold the same value, while the parameter c_7 only has 80% of its original value.

The results of the experimental tests are mainly shown in terms of load versus displacement curves (shear force versus link rotation), fracture locations, and initial propagations. The shear force is the force that acts on the shear link and can be calculated as the sum of the reaction forces in the two load cells that support the beam. The rotation represents the rotation of the shear link, which can be determined by the displacement difference between the two link ends over link length.

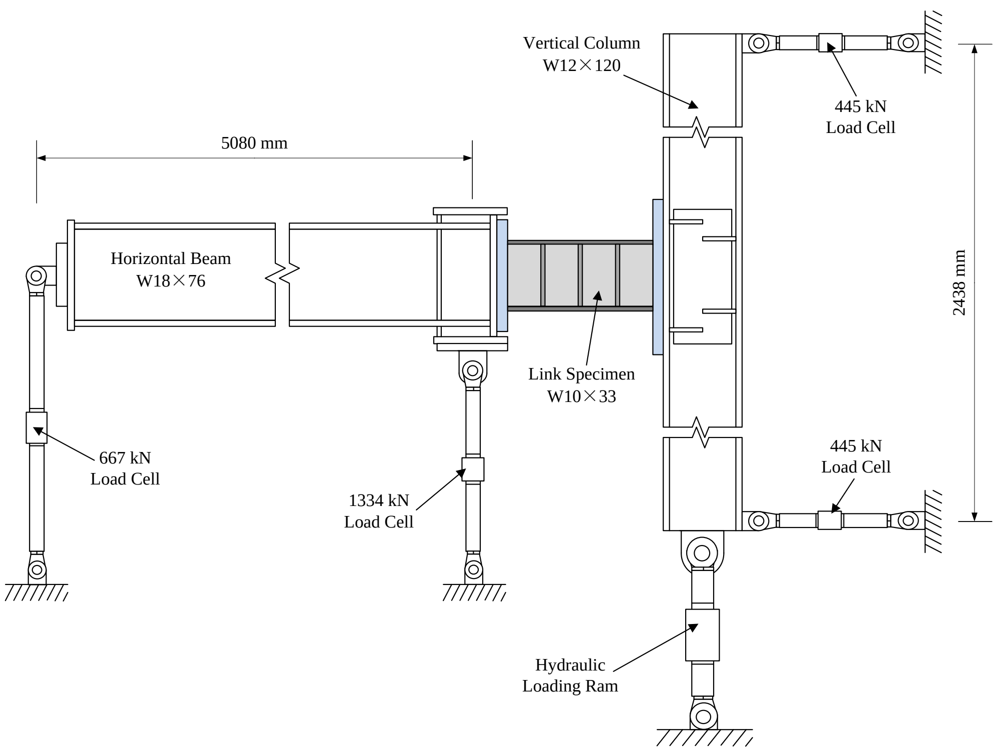

Figure 4.1 Details and dimensions of the test setup of the experimental program in Gálvez (2004), Okazaki (2004) and Okazaki et al., (2005) [Redrawn from Gálvez (2004)]

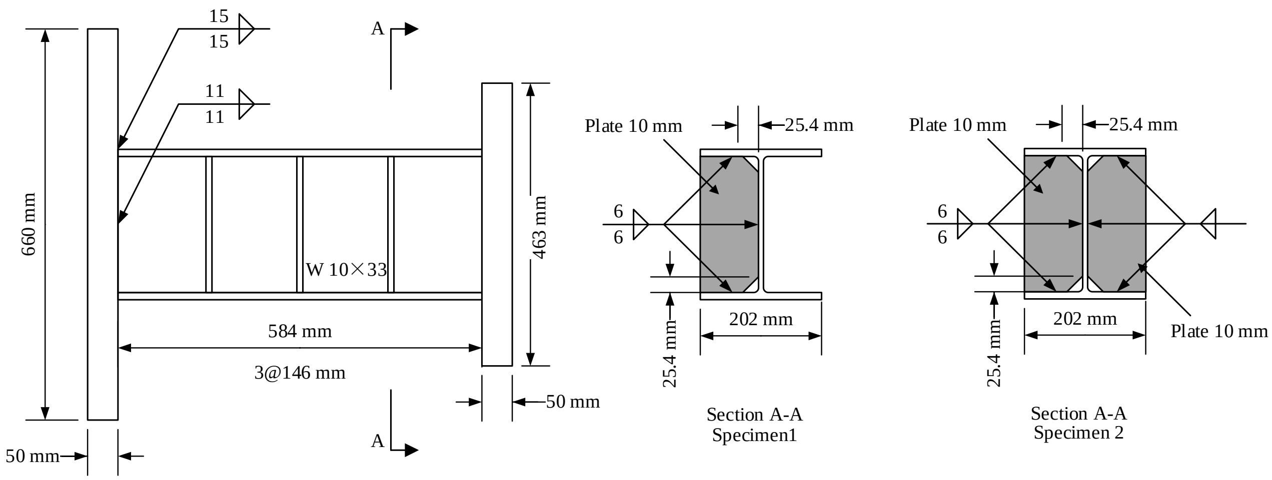

Figure 4.2 Geometry configurations and welding details for (a) specimen 1 [corresponding to specimen 5 and 8 in Gálvez (2004)] and (b) specimen 2 [corresponding to specimen 1, 2, and 3 in Gálvez (2004)]

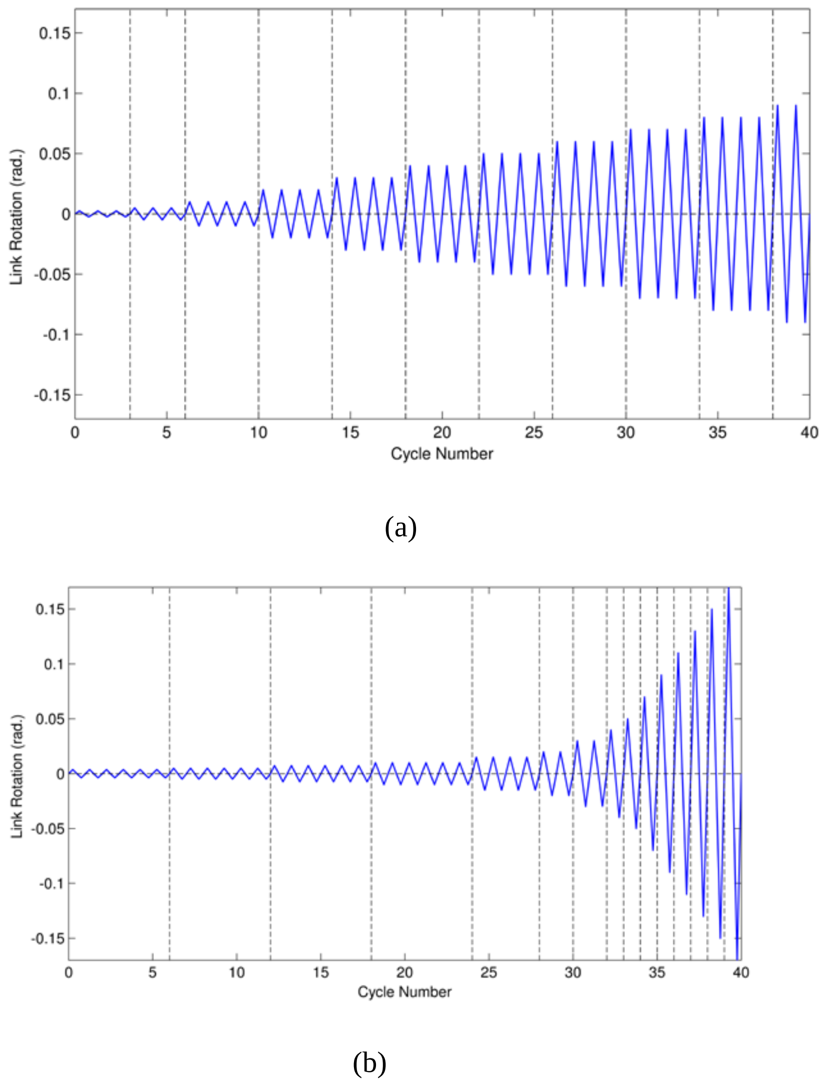

Figure 4.3 Loading protocols and failure initiation locations: (a) severe loading protocol (SLP); and (b) revised loading protocol (RLP) by Richards and Uang (2003)

4.2.2 Numerical Modeling of Selected Specimens

The general finite element (FE) program ABAQUS/Explicit (Simulia, 2012) was employed in the numerical simulations in this section. The simulated specimens include specimens with out-of-plane deformations and subsequent strong web-stiffener interactions (specimen 1), or welding on web stiffener (specimen 2), whose effects on the damage evolution cannot be ignored and make the modeling procedure more complicated.

4.2.3 Modeling Approach

For the purpose of reducing the computation demand, a multi-scale modeling technique is adopted. As shown in Figure 6.10, the beam and column are modeled using 3D beam element B31, while the link is modeled with 3D shell element S4R, and the weldments are modeled with 3D solid element C3D6T, in order to include the heat effects from welding. The beam and link are connected through coupling constraint, and the column is attached to the link by a series of multi-point constraints (MPCs). In specimen 1, since the stiffeners only "touch" the web, and out-of-plane deformations occur on web in the last several cycles before fracture, strong interactions between stiffener edges and web is present, and contact is built to simulate these interactions. A friction coefficient of 0.3, representing Class C slip factor for untreated hot rolled steel per the 2010 AISC Specifications (AISC LRFD, 2010), is adopted in these contact simulations. It is assumed that, initially, there exists a gap of 0.64 mm between the stiffener edges and link web in order to represent the fabrication tolerances. In specimen 2, the stiffeners are welded to the web, and the weldment configurations can be reached in Figure 4.2 (b). In the simulations, the weldment is modeled by a solid element, and solid-shell coupling is achieved through MPC between corresponding nodes for the constraint between weldments and web/stiffeners. The heat effects form welding on the base metal, including the effects on fracture properties. Residual stresses are discussed and defined in the following sections. Only the welding effects between the stiffeners and link web are considered, since others are insignificant for the fracture and deformation behavior, and therefore welding in other locations is simply treated as fixed boundary conditions. The hardening parameters are defined in Equation 4.1, and the yielding stresses are 350 Mpa for specimen 1, and 381 Mpa for specimen 2.

$$dr = 117.2 \times (5 - r)dp$$

$$d\boldsymbol{\alpha} = \frac{2}{3} \times 3447 \times d\boldsymbol{\varepsilon}^{pl} - 38 \times \boldsymbol{\alpha} dp \tag{4.1}$$

Loading procedures in the simulation exactly followed the equivalents in the corresponding laboratory tests, in which specimen 2 is subjected to the severe loading protocol (SLP) and specimen 1 is subjected to the revised loading protocol (RLP). The loads are applied through the displacement Δ_3 on the two ends of the column, shown in Figure 6.10. Similar to their experimental equivalents, the loads applied are measured from the sum of the reaction forces at the two pinned boundary conditions of the beam, F_1+F_2, and the link rotations are calculated through the ratio between the difference of displacements at the center elements of the link web at two ends, Δ_1 and Δ_2, and the link displacement L, which equals 584 mm in the present study.

Since buckling occurred in the specimen without welding between the web and stiffeners, geometric nonlinearities are considered through large strain–large displacement formulation. The geometric imperfections are introduced in the analysis in order to trigger the out-of-plane web deformations in certain loading cycles. An Eigen analysis by ABAQUS Standard buckling analysis is first conducted in order to determine the buckled modes of the link web when subjected to applied loads, and then according to comparisons with experimental results of web buckling, an appropriate buckled shape is identified. The maximum value of geometric imperfection of the link web is scaled to 2.5 mm (0.1 inches), based on the suggestions by El-Tawil et al. (1998), which is reasonable compared with the total out-of-plane fabrication straightness tolerances for W shapes in the AISC (2010) construction manual. Other geometric imperfection values are accordingly scaled. The scaled Eigen shapes are then added to the original geometry, and a new geometry with an imperfection pattern is created. In the present study, the imperfection comprises four Eigen shapes.

The fracture criterion in Equation 2.22 is applied through user-defined subroutine VUMAT, and elements whose damage variables reach 1 are deleted from the mesh. In the concerned areas of the link webs, which have high fracture possibilities, a refined mesh size with 1.5×1.5 mm resolution is employed, as shown in Figure 4.4. For the sake of computational efficiency, only the link webs' material model is defined by VUMAT, while in other parts of the model, the material models embedded in ABAQUS are adopted.

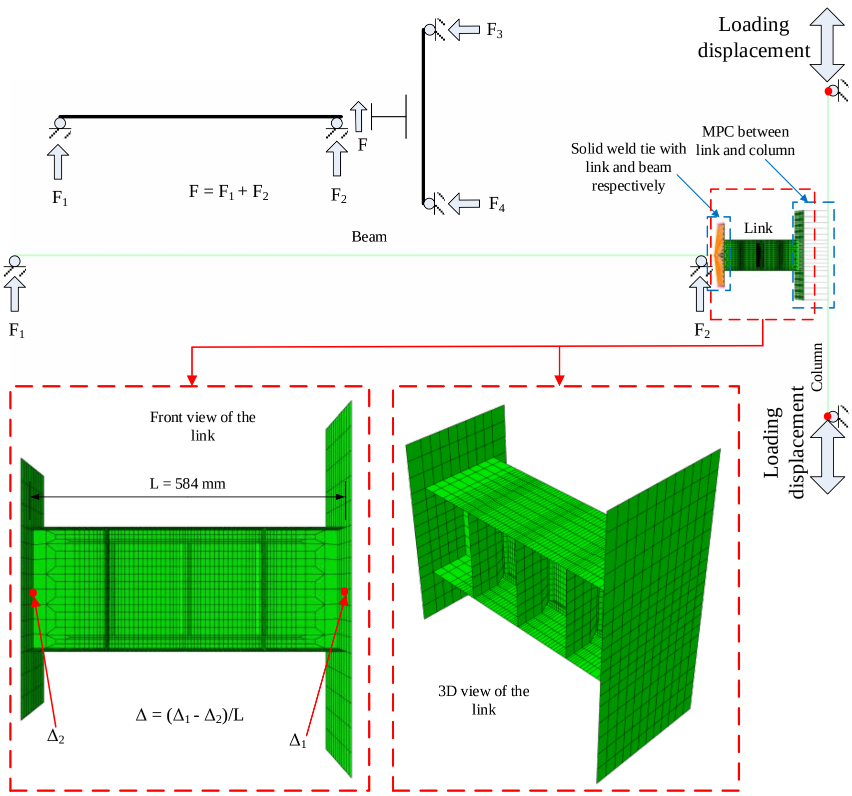

Figure 4.4 Depiction of a typical numerical model used for EBF link (Specimen 2)

4.2.4 The Heat Affected Zones (HAZ)

Although the residual stresses were proven to have an insignificant effect on ductile fracture, the fracture resistance of welded structures is admittedly degraded, which causes ductility to be one of the main concerns for this structure type. The degradation actually comes from the exposure to temperature during the welding process.

The heat affected zone (HAZ) is the area of base metal that does not melt but has its microstructure and mechanical properties altered by the intensive heat from the heat related processes, such as welding and hot cutting operations. The heating and subsequent cooling process both cause the change within the zones from weld interface to the boundary of the sensitizing temperature of the base metal. The extent of change depends on many factors, primarily including the heat amount and input rate, the cooling environment, and the related metals.

Many common mechanical properties, including yielding stress, modulus, ductility, and hardness change after the material experiences thermo-cycles. Since the characteristics of these cycles vary as a function of the distance from the heat source, the material at the HAZ becomes heterogeneous. Therefore, the material and damage parameters calibrated for the base metal cannot be directly applied to the HAZ material. However, compared with all the components, the relative dimension of the HAZ is very small, and hence the global behavior of the link will be not greatly influenced by altering the material in the HAZ, except in terms of the failure/fracture phenomenon where local crack initiation may be located in the HAZ. Since the HAZ is greatly restrained and usually does not exceed the web thickness, corresponding to one meshed element of 1.5 mm x 1.5 mm in present numerical models, the material property change of HAZ is insignificant, and the material properties of the single element are averaged from the HAZ and the other base or transitional material. Therefore, the material change in HAZ is not accounted for directly, but compensated for in the damage parameter change.

Generally, the resistance to fracture in the HAZ is degraded by thermal cycles, and the loss of fracture capacity, sometimes described as loss of toughness in the perspective of traditional fracture mechanics, is mainly due to the formation of local brittle zones, which are believed to be due to the presence of martensite- austenite (M-A) islands. The microstructure of the base metal will be changed if the thermal cycles exceed some certain transformation temperature in the HAZ. As shown in Figure 4.5 (a), for a single pass weld, the HAZ microstructures can be broadly categorized into four regions, and with the experienced temperature descending from the weld interface into the base metal, these are (1) coarse grain HAZ (CG HAZ), (2) fine grain HAZ (FG HAZ), (3) intercritical HAZ (IC HAZ) or partially transformed HAZ, and (4) subcritical HAZ (SC HAZ) or tempered HAZ. There are no sharp transitions between each zone. The microstructure of the HAZ is very complicated. For low-carbon steels, whose original microstructure is the ferrite/pearlite, in the CG HAZ the original steel is transformed and more or less characterized by quenched microstructure of bainite/martensite, and austenite grain also grows with increasing peak temperature, then followed by a subsequent microstructure coarsening; the FG HAZ is featured with a fine ferrite grain structure, from the normalizing heat treatment; in IC HAZ, the pearlite is only partially transformed to ferrite due to the reduced temperature; while in SC HAZ, there is no microstructure change since the temperature is not high enough, and the base metal only undergoes a thermal treatment. In the case of a multi-pass weld, the HAZ are reheated by the subsequent cycles, and the microstructure may be altered again significantly with a more complicated transformation mechanism and more regions produced. The difference between single-pass and multi-pass welds lies in the fact that the original microstructure has transformed from the original ferrite/pearlite to possibly the bainite/martensite of CG HAZ. With another high thermal cycle, more martensite and austenite forms, which means that more M-A brittle islands are produced. It has been noted that the intercritically reheated coarse grain HAZ (IRCG HAZ) is the most degraded zone among these regions (Homma et al., 1998), as shown in Figure 4.5 (b), which shows the classifications for a multi-pass weld.

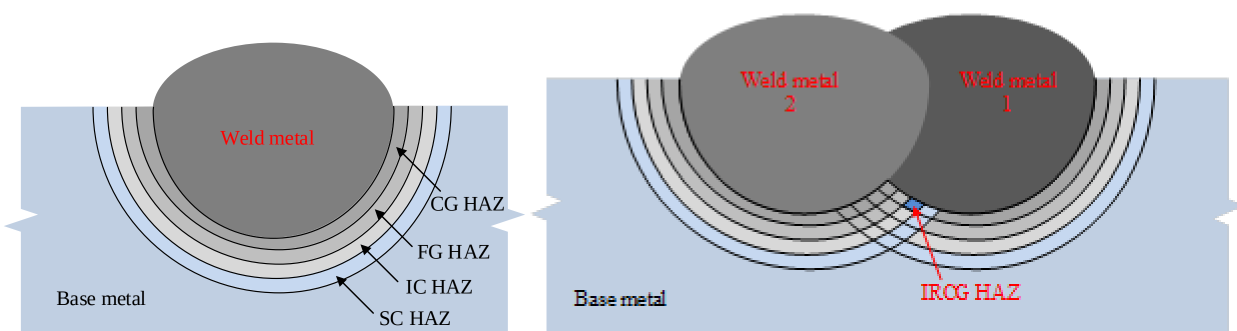

(a) (b)

Figure 4.5 Classification of HAZ: (a) single-pass weld, and (b) multi-pass weld

There is no well-accepted quantitative definition on the degradation amount of fracture resistance in HAZs, and the related studies are scarce and feature diverse conclusions. For ULCF or ductile fracture, Tateishi and Hanji (2004) indicated that the crack initiation life in HAZ was only around 30% of that of the base metal. Liao et al. (2012), on the other hand, only found a slight degradation, which might be attributed to the fact that the samples included a wide range of material ranging from HAZ to base metal. In the present study, the degradation factor for damage parameters of certain HAZ locations is qualitatively calibrated and implemented in the numerical simulations, and no attempts are performed to quantify a general degradation factor for structural steel. However, the quantification of such merits extensive study in the future. The degradation factor for HAZ under single pass welding is calibrated as

0.8, and for HAZ under two-pass welding it is 0.8×0.8=0.64. Further study should be conducted in order to quantitatively calibrate the degradation factors for common steel under regular welding procedures.

4.2.5 Simulation Results of Shear Links

The corresponding laboratory tests were evaluated mainly from the load-displacement curves, buckling behavior, fracture initiation, and propagation perspective. Thus, the numerical simulations conducted in this study provide equivalent results in order to validate the damage model, numerical modeling, and simulation procedure. Detailed discussions of the results are listed below. Additional results can be found in Wen and Mahmoud (2018).

The numerical simulation procedure is first verified by comparisons between numerical and experimental load-displacement curves. As previously stated, the load in this case is the shear force applied on the EBF link, which can be calculated by the sum of the two reaction forces on the beam, and the displacement is monitored through the rotations of the link, determined by the displacement difference between two link ends over the link length. As shown in Figure 4.6 (a) and (b), both the curves correlate exceptionally well with their experimental equivalents. The simulation of specimen 1 did not extend far into the propagation stage, while specimen 2 was simulated until almost complete web failure. Although in specimen 1, the stiffeners are not rigidly tied to the web, web out-of-plane deformations are still well restrained since there is no obvious softening in the load versus displacement curves. In the monotonic cases discussed in Chapter 3, the fracture was usually indicated by a sudden drop of the load versus displacement curve, but in the cyclic loading cases, this was not the case. As shown in Figure 4.6 (b), fracture initiated at the last cycle of step 8 (-0.06 rad.), and the fracture propagated thereafter, but only in the third cycle of step 9 did the load versus displacement curve start to “soften” and drop. The curves for shear force versus inelastic/plastic rotations are depicted in Figure 4.6 (a) and (b) for the two specimens, since the inelastic/plastic rotation is usually used for assessment of link resistance to failure, and the inelastic/plastic rotation γ_p can be determined by Equation 4.2 as follows

$$\gamma_p = \gamma - \frac{V}{K}, \qquad (4.2)$$

where γ is the total rotation, V is the link shear force, K is the elastic rotation stiffness, computed from the ratio of V and γ in elastic cycles, which are the cycles in the first two steps in the present study.

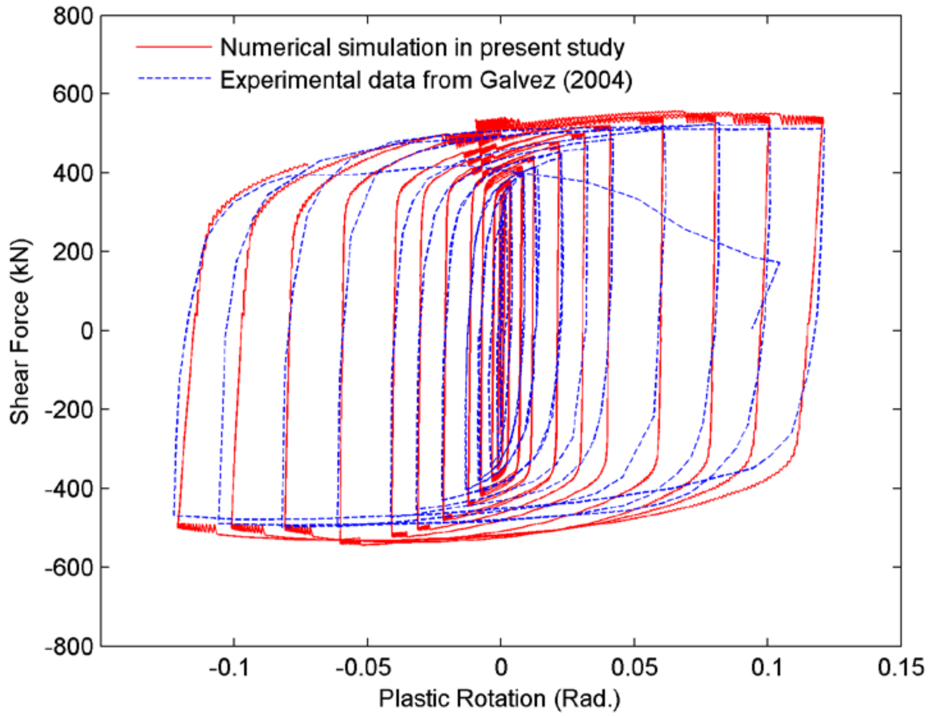

(a)

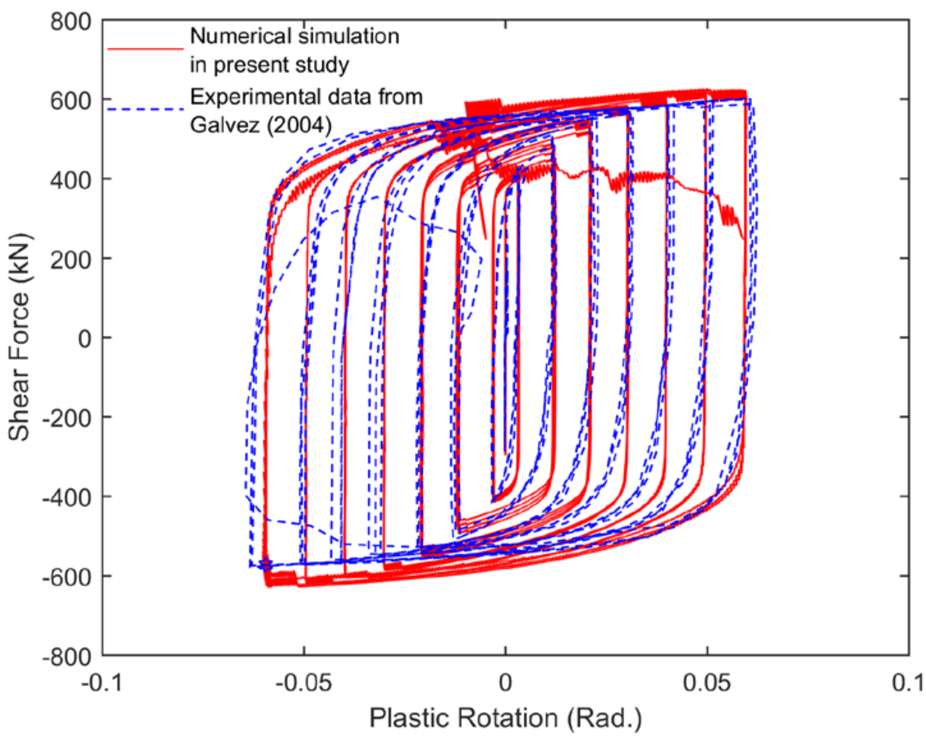

(b)

Figure 4.6 Comparisons on link shear force versus plastic rotation curves in numerical simulations and laboratory tests: (a) Specimen 1, and (c) Specimen 2. (Experimental data from Gálvez [2004])

Comparisons of fracture initiation between the numerical simulations and experimental tests are shown in Figure 4.7 (a), (b) and (c), and (d), respectively, for specimens 1 and 2. For specimen 1, whose stiffeners are not tied to web, web fracture initiates in an abrupt manner due to the rubbing from the center stiffener. The out-of-plane deformations of the web eventually start the interactions between web stiffeners, as shown in Figure 4.7 (a) and (b), and the interactions become stronger with increasing web out-of-plane deformations. Therefore, there exists strong local deformations on the web, which induces local damage concentrated zones; subsequently, the zones will fracture, although the damage level at other areas is still not significant. In this case, web out-of-plane deformations play a significant role, and hence fracture initiation is depicted in the contour of web out-of-plane deformations. For specimen 2, with stiffeners welded to web, there is only negligible web out-of-plane deformation, and the damage develops mainly because of in-plane stress/strain fields. As previously stated, the fracture resistance of HAZs is severely degraded, especially for HAZs that undergo multi-pass welding influences, which, in this case, is the weld toe of the stiffeners toes on link web. As expected, fracture initiates at the intersection of the two weld terminations, as shown in Figure 4.7 (c) and (d), and starts to propagate from the intersection locations. As shown in Figure 6.17, the numerical simulations agree well with their experimental equivalents.

As the propagation starts, there is no abrupt progression of fracture, unlike the cases under monotonic loading conditions in Chapter 3. During the cycle after fracture initiation, the first cycle of step 9, the propagation is still mainly concentrated at the intersection of the two weld terminations where fracture initiates. At the second cycle and most of third cycle of step 9, fracture starts to propagate in a stable and horizontal manner along the line of two weld termination intersections, as shown in Figure 4.8 (a). When entering the latter stage of the third cycle, fracture starts to progress unstably and abruptly and also prorogates vertically along the single pass HAZs, as shown in Figure 4.8 (b). The final fracture almost vertically cuts the web into two pieces. As shown in Figure 4.8, all the numerical simulations correlate well with corresponding fracture phenomenon in laboratory tests.

4.2.6 Discussion of Results

As stated above, numerical simulations agree well with the experimental results in the perspective of load versus displacement curves, buckling behavior, fracture initiations, and propagations. Therefore, it can be concluded that the procedure of numerical simulation, with the newly developed fracture criterion in Chapter 2, is appropriate for predicting the full response of the steel structural details. The welding process brings deleterious effects to the base metal, at least in the perspective of fracture resistance, which therefore should be considered in the prediction procedures. The stiffeners not welded to the web can still restrain the out-of-plane deformations, but the restraint-induced interaction can also be detrimental to the fracture resistance of the web.

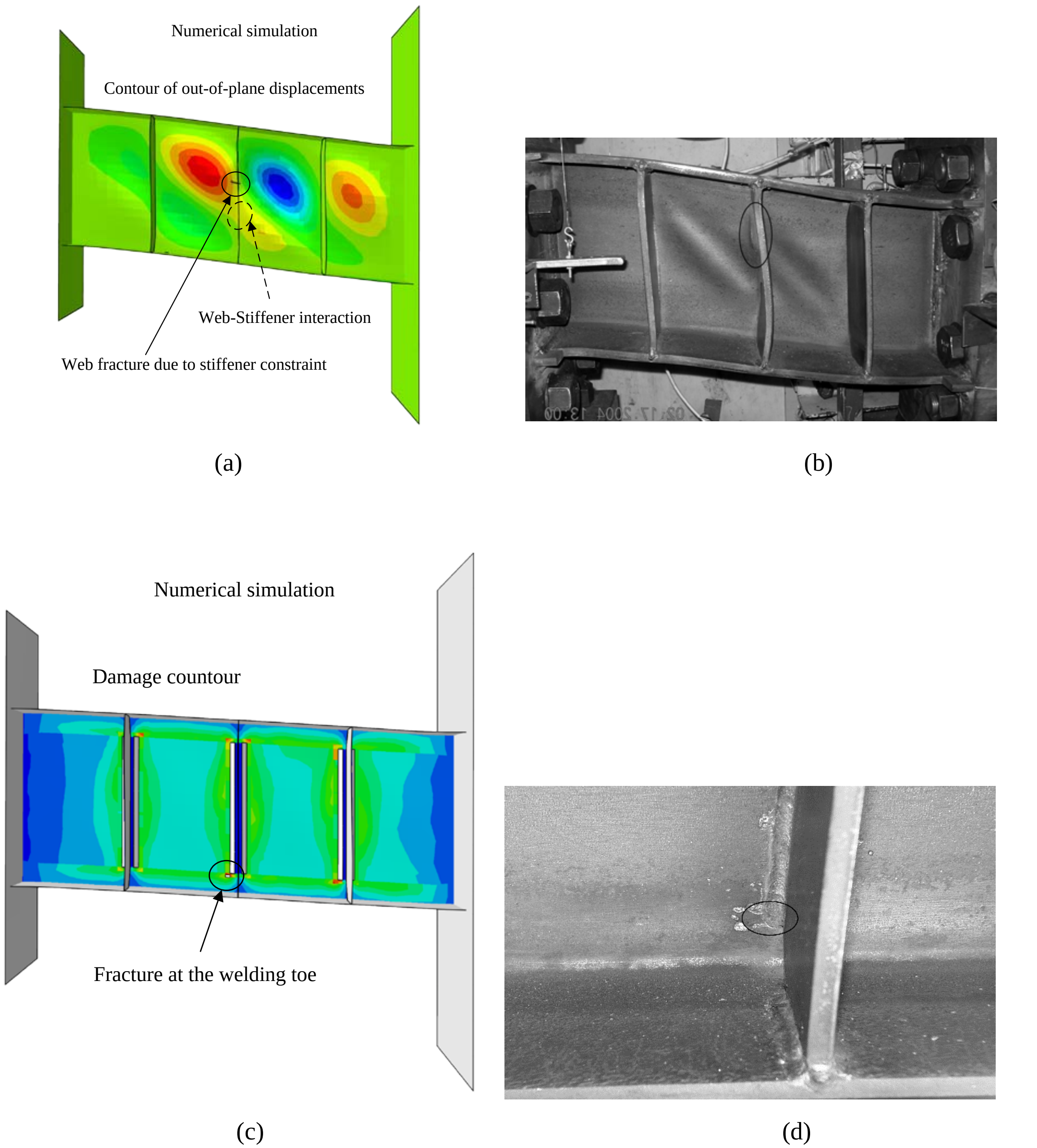

Figure 4.7 Comparisons on shear link fracture initiation between numerical simulations and laboratory tests: (a) simulation of specimen 1, (b) experiment of specimen 1, (c) simulation of specimen 2, and (c) experiment of specimen 2. (Experimental photos from Gálvez [2004])

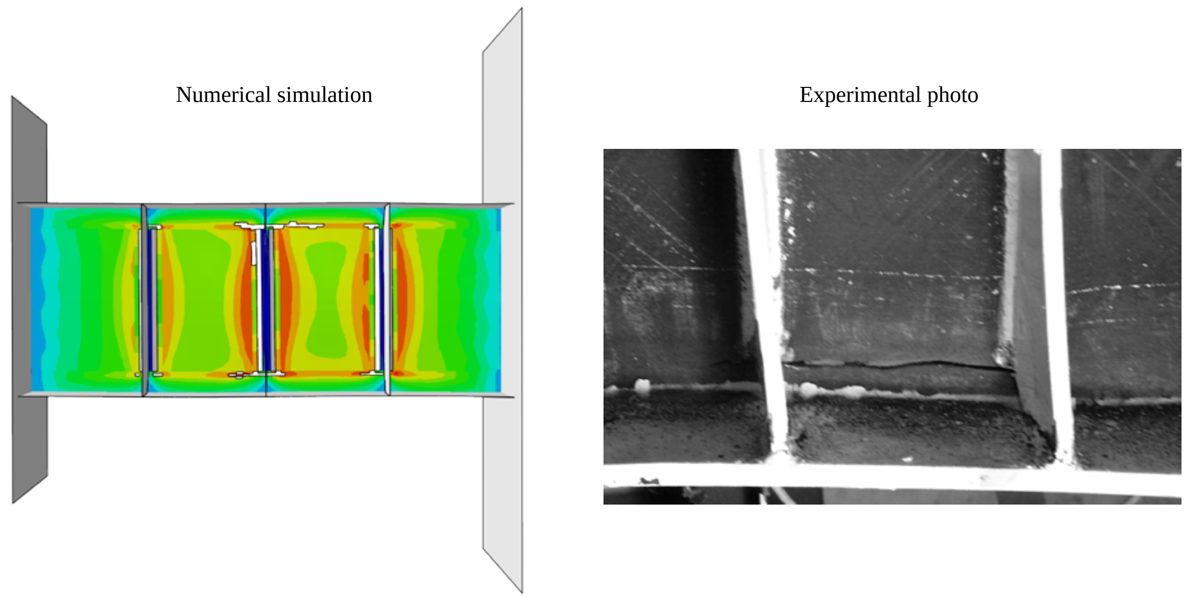

(a)

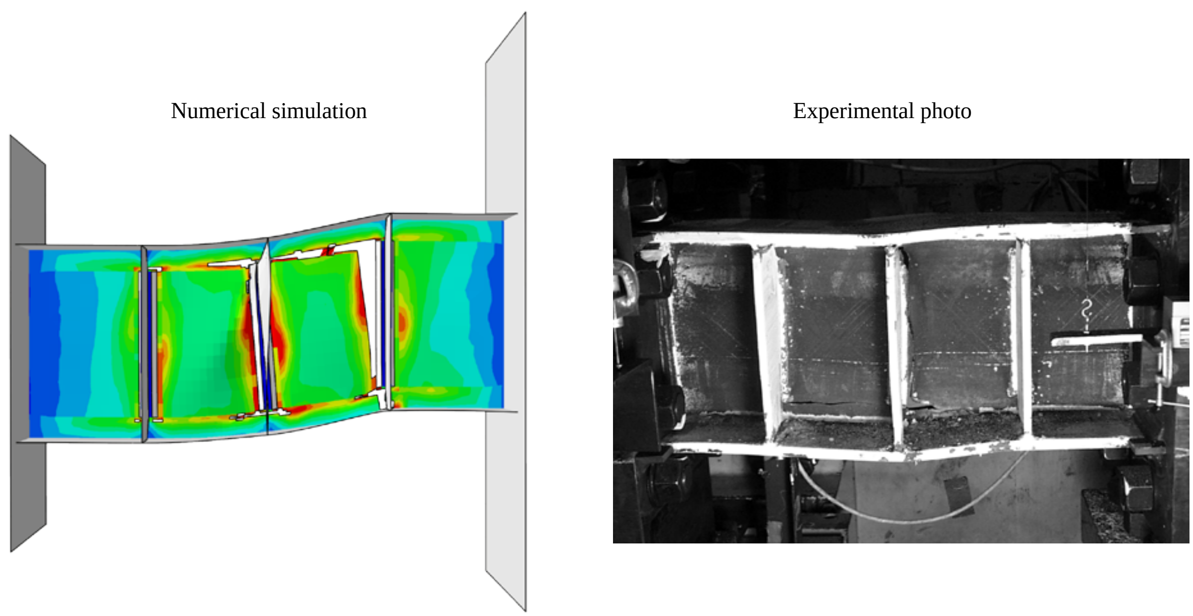

(b)

Figure 4.8 Comparisons on shear link fracture propagation between numerical simulations and laboratory tests: (a) horizontal crack after completing the second cycle of load step 9, and (b) final fracture. (Experimental photos from Gálvez [2004])

4.3 Concluding Remarks

In this section, the main objective is to implement the fracture criterion designed for reverse loadings conditions. Since the user-defined damage variables could not be applied in the adopted finite element tool, ABAQUS, a user-defined material subroutine VUMAT was programmed through a newly derived implicit radical return integration algorithm for the combined hardening material model. The VUMAT was validated through comparisons with equivalent material models embedded in ABAQUS. The objective for the implementation is to investigate and predict the response of three shear links in typical eccentric braced frames, which have been experimentally tested by Gálvez (2002). The final fracture of one of the links is not dependent on the welding process but rather on buckling of the link web, and the fracture of the other specimens is highly dependent on the welding that connects the stiffener to the web. Multiscale numerical models were built to simulate all these features. The effects of welding induced residual stress and fracture resistance degradation in HAZs were also explored. It was noted that the effects of residual stress are insignificant for fracture under cyclic loadings with large elastic deformations, since the induced stress fields are relaxed only after several loading cycles, while fracture resistance is significantly degraded due to the concentrated heat input from welding, and the loss of the resistance can reach 70%.

5. CONCLUSION AND FUTURE WORKS

The main focus of this dissertation is on the development and application of a new ductile fracture model for predicting ductile fracture under various loading conditions. Criteria pertaining to different loading cases were developed then validated against an ensemble of experimental data. The implementation of these models on structural details showed excellent agreement with experimental results, which further verified the proposed approaches. However, some aspects regarding the simulation of ductile fracture still merit further research. The main achievements of the dissertation and the possible improvements in future studies are summarized in the following section.

5.1 Summary of Main Contributions

Study on the stress triaxiality and Lode parameter effects on ductile fracture. Ductile fracture has been known to be stress triaxiality-dependent for many years, but the role of the Lode parameter has not been realized until very recently. In the present study, the effects of stress triaxiality and Lode parameter are explored. The two dependencies, which also refer to two kinds of work hardening damage due to hydrostatic and deviatoric stress components, respectively, are always present in any range of stress states except the cut-off region. However, the relative contribution of the two dependencies to the total damage varies with different stress states. With increasing stress triaxialities, the damage due to hydrostatic stress becomes more significant, while the deviatoric stress portion decreases in terms of its relative contribution, and vice versa. Based on the above conclusion, a three/four parameter ductile fracture model is proposed, with the concept that the magnitude of the stress triaxiality dependency is altered by the presence of the Lode parameter. In the newly developed model, the corresponding fracture strain locus map is shown to exhibit a decreasing exponential function of the stress triaxiality coupled with an asymmetric cosine function of the Lode parameter. The newly proposed criterion is validated through comparisons between the predicted fracture strains and experimental data obtained from the literature for various types of aluminum alloys and steel grades, and good agreements have been achieved. During the verification analysis, it is also shown that the extent of the two dependencies varies with different metals, and some metals are only sensitive to stress triaxiality. The proposed model also demonstrates advantages over existing known ductile fracture criteria as shown in the comparisons.

Simulation of the block shear fracture failure in steel connections. Block shear failure is usually featured with simultaneous tensile and shear fracture, which correspond to stress triaxiality and Lode parameter, respectively. Therefore, block shear failure is appropriate for the implementation and further validation of the newly proposed ductile fracture criterion. Numerical simulations on the full response of gusset plate and coped beam connections are conducted up to and including the entire block shear failure. Accuracy of the modeling approach and implementation of the ductile fracture model are verified through comparisons between the numerical results and existing experimental data in terms of load versus displacement curves, fracture profiles, and fracture sequences. Through the numerical simulations, the inherent mechanisms of block shear in gusset plate and coped beam connections are explored and discussed, some of which are actually explained physically for the first time.

Parametric studies of geometrical effects on block shear failure. The parametric study focused on the geometric effects on fracture behavior through the verified numerical simulation procedure. The geometric variables include bolt spacing on the tensile and shear planes, and bolt edge/end distances, most of which have not been fully explored by laboratory tests in the past. Some new and relevant findings are reached for the first time. Three different block-shear failure modes and one bolt hole tear out mode are captured in the simulations, including “tensile fracture + shear yielding,” “tensile fracture + shear fracture,” “tensile yielding + shear fracture,” and hole tearout fracture. The classifications of the four fracture modes vary with combinations of bolt hole spacing on the shear and tensile planes. The first two failure modes are desired in design and typically dominate in practice because of the practicality of the hole spacing, while the other two should be avoided. These findings are beneficial and suggested for the design code development.

Nonlinear and loading history effect on ductile fracture. Fracture after few reverse loading cycles, or ULCF, share similar underlying mechanisms with ductile fracture under monotonic loading, and therefore can be modeled through the extension of monotonic loading ductile fracture criteria. The newly proposed ductile fracture model, with stress triaxiality and Lode parameter dependencies, serves as the base model for cyclic load extension that includes damage evolution and loading history. The nonlinear damage evolution rule is proposed and compared with the linear one that is typically employed in popular ductile fracture models for monotonic loading. The loading history effects, which are unique to reverse/cyclic loading cases, are explored through the introduction of a new parameter, which is determined through stress and back stress components. Two damage evolution models, based on the nonlinearity and history effects, respectively, are developed, and a new combined criterion with consideration of both nonlinearity and history effects is proposed and validated through comparisons between the predictions and corresponding experimental results. For the combined model and the model with only history effects, satisfactory correlations are achieved, but not for the criterion with only nonlinearity. Therefore, it is suggested that the combined approach be utilized in the application of metal fracture predictions under cyclic loading, and the history effect modified approach may serve as a backup choice. The analyses showed that the extent of dependencies on nonlinearity and history effects varies with different metals and steel grades.

Application of newly developed fracture criterion to steel structures under cyclic loading. It is essential to predict the full response of structures under cyclic loading with large inelastic deformations, especially at the onset of the fracture. However, it is usually cumbersome to perform the fracture simulation since available fracture prediction models are scarce. The attempts to simulate to fracture under reverse loadings conditions by using the newly developed fracture model geared on the reverse loading conditions are conducted in this study through the simulations of the full response of shear link in EBF, up to and including the entire fracture. To include the fracture-associated variables, an implicit integration algorithm is derived for the material constitutive equations with combined hardening, accompanied by a user-defined material subroutine, VUMAT, programmed and validated using specimens at different scales. Simulation results are compared with corresponding experimental results in terms of load versus displacement curves, fracture locations, and profiles. Excellent agreements are achieved, which validated the numerical simulation procedure and also further verified the developed fracture criterion designed for cyclic loading situations, in addition to validations on the specimen level.

5.2 Suggestions for Future Studies

Although comprehensive analyses have been performed in this dissertation on ductile fracture under various stress states and loading conditions, the following topics are suggested for future explorations in order to further develop the entire fracture prediction approach.

- *Nonlocal fracture model*. As stated, fracture simulation in the present study is mesh or locally dependent, and therefore accurate predictions of fracture initiations/propagations require the structural details to be meshed appropriately. This highly depends on the researchers' experiences and expertise. Therefore, the development of a non-local fracture criterion is more desired to streamline the application of the model.

- *General quantitative definition on fracture resistance degradation at HAZ*. In the present study, the degradation of fracture resistance in single or multi pass HAZ is only roughly determined, which is more likely to serve qualitative examples in the future. The problem of degraded fracture resistance is very critical in many welded structures. A general quantitative definition on the extent of degradation on the fracture resistance at various types of HAZ is highly desired.

- *Damage parameter calibration*. Although there are many metal types and steel grades whose damage parameters have been calibrated in this dissertation, the parameters for the majority of engineering metals are still unknown. Therefore, in order to predict full response of structures using these types of metals, it is desired that the damage parameters, or associated fracture strain under various stress states, be determined and calibrated before use, at least for major structural steels.

6. REFERENCES

Aalberg, A., and Larsen, P. K. (1999) “Strength and Ductility of Bolted Connections in Normal and High Strength Steels.” Department of Structural Engineering, Norwegian University of Science and Technology, N-7034, Trondheim, Norway.

American Institute of Steel Construction (1999). “Load and Resistance Factor Design Specification.” Chicago, IL, USA.

American Institute of Steel Construction (2010). “Load and resistance factor design specification for structural steel buildings.” Chicago, IL, USA.

Anderson, T. L. (1995). Fracture Mechanics, 2nd Edition. CRC Press, Boca Raton, FL.

Arce, G. (2002). “Impact of higher strength steels on local buckling and overstrength of links in eccentrically braced frames.” Master’s thesis, University of Texas at Austin, Austin, TX.

Argon, A. S., and Im, J. (1975). “Separation of second phase particles in spheroidized 1045 steel, Cu-0.6pct Cr Alloy, and maraging steel in plastic straining.” *Metallurgical Transactions* 6A, 839-851.

Bai, Y. (2008). “Effect of loading history in necking and fracture.” Ph.D. dissertation, Massachusetts Institute of Technology, Cambridge MA.

Bai, Y., and Wierzbicki, T. (2010). “Application of extended Mohr–Coulomb criterion to ductile fracture.” *International Journal of Fracture*, 161(1), 1-20.

Bao, Y. (2003). “Prediction of ductile track formation in uncracked bodies.” Ph.D. dissertation, Massachusetts Institute of Technology, Cambridge MA.

Bao, Y., and Treitler, R. (2004). “Ductile crack formation on notched Al2024-T351 bars under compression–tension loading.” *Materials Science and Engineering*: A, 384(1), 385-394.

Bao, Y., and Wierzbicki, T. (2004). “On fracture locus in the equivalent strain and stress triaxiality space.” *International Journal of Mechanical Sciences*, 46(1), 81-98.

Barsoum, I., and Faleskog, J. (2007). “Rupture mechanisms in combined tension and shear—experiments.” *International Journal of Solids and Structures*, 44(6), 1768-1786.

Benzerga, A., and Leblond, J. B. (2010). “Ductile fracture by void growth to coalescence.” *Advances in Applied Mechanics*, 44, 169-305.

Bermin, F. M. (1981). “Cavity formation from inclusions in ductile fracture.” *Metallurgical Transactions* 12 A, 723-731.

Birkemoe, P. C., and Gilmor, M. I. (1978). “Behavior of bearing-critical double-angle beam connections.” *Engineering Journal*, 15(4), 109-115.

Bjorhovde, R., and Chakrabarti, S. K. (1985). “Tests of full-size gusset plate connections.” *Journal of Structural Engineering*, 111(3), 667-684.

Brozzo, P., Deluca, B., and Rendina, R. (1972). “A new method for the prediction of formability limits in metal sheets.” Proceedings, 7th Biennial Conference, International Deep Drawing Research Group, Amsterdam, Netherlands.

Chu, C., and Needleman, A. (1980). “Void nucleation effects in biaxially stretched sheets.” *Journal of Engineering Materials and Technology* 102, 249-256.

Clift, S. E., Hartley, P., Sturgess, C. E. N., and Rowe, G. W. (1990). “Fracture prediction in plastic deformation processes.” *International Journal of Mechanical Sciences*, 32(1), 1-17.

Cockcroft, M. G., and Latham, D. J. (1968). “Ductility and the workability of metals.” J*ournal of the Institute of Metals*, 96(1), 33-39.

Coffin, L. (1954). “The problem of thermal stress fatigue in austenitic steels at elevated temperatures.” In Symposium on Effect of Cyclic Heating and Stressing on Metals at Elevated Temperatures. ASTM International.

Fang, C., Lam, A. C., Yam, M. C., and Seak, K. S. (2013). “Block shear strength of coped beams with single-sided bolted connection.” *Journal of Constructional Steel Research*, 86, 153-166.

Fatemi, A., and Yang, L. (1998). “Cumulative fatigue damage and life prediction theories: a survey of the state of the art for homogeneous materials.” *International Journal of Fatigue*, 20(1), 9-34.

Franchuk, C. R., Driver, R. G., and Grondin, G. Y. (2002). “Block shear behavior of coped steel beams.” Structural Engineering Report 248, Department of Civil and Environmental Engineering, University of Alberta, Edmonton, Alta., Canada.

Gálvez P. Investigation of factors affecting web fractures in shear links. Master’s thesis, University of Texas at Austin, Austin, TX, USA.

Gurson, A. L. (1977). “Continuum theory of ductile rupture by void nucleation and growth: Part I–Yield criteria and flow rules for porous ductile media.” *Journal of Engineering Materials and Technology* 99(1), 2-15.

Hardash, S. G. (1984). “Gusset plate design utilizing block-shear concepts.” The Department of Civil Engineering and Engineering Mechanics, University of Arizona, Tucson, Arizona.

Homma, K., Miki, C., and Yang, H. (1998). “Fracture toughness of cold worked and simulated heat affected structural steel.” *Engineering Fracture Mechanics*, 59(1), 17-28.

Huns, B.B.S., Grondin, G.Y., and Driver, R.G. (2002). “Block shear behavior of bolted gusset plates.” Structural Engineering Report No. 248, Department of Civil Engineering, University of Alberta, Edmonton, Alta., Canada.

Johnson, G. R., and Cook, W. H. (1985). “Fracture characteristics of three metals subjected to various strains, strain rates, temperatures and pressures.” *Engineering Fracture Mechanics*, 21(1), 31-48.

Kanvinde, A. M., and Deierlein, G. G. (2007). “Cyclic void growth model to assess ductile fracture initiation in structural steels due to ultra-low cycle fatigue.” *Journal of Engineering Mechanics*, 133(6), 701-712.

Ko, Y. K., Lee, J. S., Huh, H., Kim, H. K., and Park, S. H. (2007). "Prediction of fracture in hub-hole expanding process using a new ductile fracture criterion." *Journal of Materials Processing Technology*, 187, 358-362.

Kuroda, M. (2001). "Extremely low cycle fatigue life prediction based on a new cumulative fatigue damage model." *International Journal of Fatigue* 24, 699-703.

Kuwamura, H., and Yamamoto, K. (1997), "Ductile crack as a trigger of brittle fracture in steel," *Journal of Structural Engineering*, June, 1997, 729-735.

Lam, A. C., Fang, C., Yam, M. C., Wang, W., and Iu, V. P. (2015). "Block shear strength and design of coped beams with double bolt-line connections." *Engineering Structures*, 100, 293-307.

Lee, B. J., and Mear, M. E. (1999). "Stress concentration induced by an elastic spheroidal particle in a plastically deforming solid." *Journal of the Mechanics and Physics of Solids* 47(6), 1301-1336.

Li, H., Fu, M. W., Lu, J., and Yang, H. (2011). "Ductile fracture: experiments and computations." *International Journal of Plasticity*, 27(2), 147-180.

Lou, Y., Huh, H., Lim, S., and Pack, K. (2012). "New ductile fracture criterion for prediction of fracture forming limit diagrams of sheet metals." *International Journal of Solids and Structures*, 49(25), 3605-3615.

Manson, S. S. (1965). "Fatigue: a complex subject—some simple approximations." *Experimental Mechanics*, 5(7), 193-226.

McClintock, F. A. (1968). "A criterion for ductile fracture by the growth of holes." *Journal of Applied Mechanics*, 35(2), 363-371.

Miners, J. W. (1957). "On structural fatigue under random loading." *The Journal of the Acoustical Society of America*, 29(1), 176-176.

Nahshon, K., and Hutchinson, J. W. (2008). "Modification of the Gurson model for shear failure." *European Journal of Mechanics-A/Solids*, 27(1), 1-17.

Nast, T. E., Grondin, G. Y. and Cheng, J. J. R. (1999) "Cyclic Behavior of Stiffened Gusset Plate-Brace Member Assemblies," Structural Engineering Report 229, Department of Civil and Environmental Engineering, University of Alberta, Edmonton, Alberta, Canada.

Oh, S. I., Chen, C. C., and Kobayashi, S. (1979). "Ductile fracture in axisymmetric extrusion and drawing—part 2: workability in extrusion and drawing." *Journal of Engineering for Industry*, 101(1), 36-44.

Okazaki, T. (2004). "Seismic performance of link-to-column connections in steel eccentrically braced frames." Ph.D. dissertation, University of Texas at Austin, Austin, TX, USA.

Okazaki, T., Arce, G., Ryu, H. C., and Engelhardt, M. D. (2005). "Experimental study of local buckling, overstrength, and fracture of links in eccentrically braced frames." *Journal of Structural Engineering*, 131(10), 1526-1535.

Okazaki, T., and Engelhardt, M. D. (2007). "Cyclic loading behavior of EBF links constructed of ASTM A992 steel." *Journal of Constructional Steel Research*, 63(6), 751-765.

Oyane, M., Sato, T., Okimoto, K., and Shima, S. (1980). "Criteria for ductile fracture and their applications." *Journal of Mechanical Working Technology*, 4(1), 65-81.

Paris, P. C., Gomez, M. P., and Anderson, W. E. (1961). "A rational analytic theory of fatigue." *The Trend in Engineering*, 13(1), 9-14.

Pyttel, B., Schwerdt, D., and Berger, C. (2011). "Very high cycle fatigue–is there a fatigue limit?" *International Journal of Fatigue*, 33(1), 49-58.

Rex, C. O., and Easterling, W. S. (2003). "Behavior and modeling of a bolt bearing on a single plate." *Journal of Structural Engineering*, 129(6), 792-800.

Rice, J. R. (1968). "A Path Independent Integral and the Approximate Analysis of Strain Concentration for Notches and Cracks." *Journal of Applied Mechanics*, 35, 379-386.

Rice, J. R., and Tracey, D. M. (1969). "On the enlargement of voids in triaxial stress fields." *Journal of the Mechanics and Physics of Solids* 17(3), 201-217.

Richards, P., and Uang, C. M. (2003). "Development of testing protocol for short links in eccentrically braced frames." Department of Structural Engineering, University of California, San Diego, CA.

Ricles, J. R., and Yura, J. A. (1983) "Strength of Double-Row Bolted Web Connections." *Journal of Structural Division*, ASCE, No.ST1, Vol.109, 126-142.

Simulia, Dassault Systèmes. ABAQUS FEA Version 6.12 [Computer software]. Providence, RI. 2012.

Stoughton, T. B., and Yoon, J. W. (2011). "A new approach for failure criterion for sheet metals." *International Journal of Plasticity*, 27(3), 440-459.

Tateishi, K., and Hanji, T. (2004). "Low cycle fatigue strength of butt-welded steel joint by means of new testing system with image technique." *International Journal of Fatigue*, 26(12), 1349-1356.

Tateishi, K., Hanji, T., and Minami, K. (2007). "A prediction model for extremely low cycle fatigue strength of structural steel." *International Journal of Fatigue*, 29, 887-896.

Weck, A., Wilkinson, D. S., Maire, E., and Toda, H. (2008). "Visualization by X-ray tomography of void growth and coalescence leading to fracture in model materials." *Acta Materialia*, 56(12), 2919-2928.

Wen, H., and Mahmoud, H. (2016a). "New Model for Ductile Fracture of Metal Alloys. I: Monotonic Loading." *Journal of Engineering Mechanics*, 142(2), 04015088.

Wen, H., and Mahmoud, H. (2016b). "New Model for Ductile Fracture of Metal Alloys. II: Reverse Loading." *Journal of Engineering Mechanics*, 142(2), 04015089.

Wen, H., and Mahmoud, H. (2017). "Simulation of block shear fracture in bolted connections." *Journal of Constructional Steel Research* 134, 1-16.

Wen, H., and Mahmoud, H. (2017). "A New Approach to Predict Cyclic Response and Fracture of Shear Links and Eccentrically Braced Frames." *Frontiers in Built Environment* 4, 11.

Whitmore, R. E. (1952). "Experimental investigation of stresses in gusset plates." Bulletin No. 16, Engineering Experiment Station, University of Tennessee, Knoxville.

Wierzbicki, T., Bao, Y., Lee, Y. W., and Bai, Y. (2005a). “Calibration and evaluation of seven fracture models.” *International Journal of Mechanical Sciences*, 47(4), 719-743.

Wilkins, M. L., Streit, R. D., and Reaugh, J. E. (1980). “Cumulative-strain-damage model of ductile fracture: simulation and prediction of engineering fracture tests.” No. UCRL-53058), Lawrence Livermore National Lab., CA (USA); Science Applications, Inc., San Leandro, CA (USA).

Xue, L. (2008). “Constitutive modeling of void shear effect in ductile fracture of porous materials.” *Engineering Fracture Mechanics*, 75(11), 3343-66.

Xue, L., and Wierzbicki, T. (2008). “Ductile fracture initiation and propagation modeling using damage plasticity theory.” *Engineering Fracture Mechanics*, 75(11), 3276-3293.

Yura, J. A., Birkemoe, P. C. and Ricles, J. M. (1982) “Double Angle Beam Web Connections: An Experimental Study.” *Journal of the Structural Division, ASCE*, Vol. 108, No. ST2, February, pp. 311-325.